Chandra observation of NGC 4449: analysis of the X-ray emission from a dwarf starburst galaxy

Lesley K. Summers,[1]★ Ian R. Stevens,[1]★ David K. Strickland[2]★†
and Timothy M. Heckman[2]★

[1]*School of Physics & Astronomy, University of Birmingham, Edgbaston, Birmingham B15 2TT*
[2]*Department of Physics & Astronomy, The Johns Hopkins University, 3400 North Charles Street, Baltimore, MD 21218, USA*

ABSTRACT

We present *Chandra* X-ray data on the nearby Magellanic irregular dwarf starburst galaxy NGC 4449. Contributions to the X-ray emission come from discrete point sources and extended diffuse emission. The extended emission has a complex morphology with an extent of $\sim 2.4 \times 1.6$ kpc down to a flux density of 1.3×10^{-13} erg s^{-1} cm^{-2} arcmin^{-2}. The best spectral fit to this emission is obtained with an absorbed, two-temperature model giving temperatures for the two gas components of 0.28 ± 0.01 and 0.86 ± 0.04 keV, a total mass content of $\sim 10^7$ M$_\odot$ compared with a galactic mass of several 10^{10} M$_\odot$ and a total thermal energy content of $\sim 2.5 \times 10^{55}$ erg, with an average energy injection rate for the galaxy of a few 10^{41} erg s^{-1}. Comparison of the morphology of the diffuse X-ray emission with that of the observed Hα emission shows similarities in the two emissions. An expanding super-bubble is suggested by the presence of diffuse X-ray emission within what appears to be a cavity in the Hα emission. The kinematics of this bubble suggest an expansion velocity of ~ 220 km s^{-1} and a mass injection rate of ~ 0.14 M$_\odot$ yr^{-1}, but the presence of a huge H I halo ($r \sim 40$ kpc) in NGC 4449 may prevent the ejection, into the intergalactic medium, of the metal-enriched material and energy it contains.

The arcsecond resolution of *Chandra* has detected 24 X-ray point sources down to a completeness level corresponding to a flux of $\sim 2 \times 10^{-14}$ erg s^{-1} cm^{-2}, within the optical extent of NGC 4449 and analysis of their spectra has shown them to be from at least three different classes of object. As well as the known supernova remnant in this galaxy, it also harbours several X-ray binaries and supersoft sources. The point source X-ray luminosity function, for the higher-luminosity sources, has a slope of ~ -0.51, comparable to those of other starburst galaxies.

Key words: ISM: jets and outflows – galaxies: individual: NGC 4449 – galaxies: starburst – X-rays: galaxies.

1 INTRODUCTION

NGC 4449 is a nearby Magellanic dwarf irregular starburst galaxy, which has an inclination of 56.2° and a mass of $\sim 4 \times 10^{10}$ M$_\odot$ (Bajaja, Huchtmeier & Klein 1994, mass has been scaled for our assumed distance which is discussed later). As such it allows another opportunity for the study of the starburst phenomenon and its effect on galaxy evolution in the local Universe. Dwarf galaxies as the basic building blocks in the hierarchical merging cos-

mology scenario are likely to have haboured the earliest sites of star formation in the Universe and so their study in the local Universe can give insight into the evolution of such objects at high redshift. Observations of local edge-on starburst galaxies (Strickland et al. 2000; Weaver 2001) are presenting a picture of kpc-scale, soft X-ray-emitting, bi-polar outflows in the form of galactic winds transporting mass, newly synthesized heavy elements and energy into the intergalactic medium (IGM). These winds result from the pressure-driven outflows along the minor axes of these galaxies produced from the efficient thermalization of the mechanical energy from the supernovae (SNe) explosions and stellar winds of the massive stars in their OB associations and super star clusters (SSC). Inclined galaxies such as NGC 4449 containing

---

★E-mail: lks@star.sr.bham.ac.uk (LKS); irs@star.sr.bham.ac.uk (IRS); dks @pha.jhu.edu (DKS); heckman@pha.jhu.edu (TMH)
†*Chandra* Fellow.

such phenomena present a less clearly observable picture. However, observations of how absorption and temperature of the diffuse X-ray emission varies within them and links between Hα, H I and X-ray morphology suggests that a similar scenario also applies to these objects.

NGC 4449 has been observed across the electromagnetic spectrum and displays some both interesting and unusual characteristics. Radio observations have shown it to contain an extremely luminous supernova remnant (SNR) (Bignell & Seaquist 1983), a very extended H I halo (~40 kpc in radius) that appears to be rotating in the opposite direction to the gas in the core of the galaxy (Bajaja et al. 1994) and to have a large-scale ordered magnetic field (Klein et al. 1996). The angular velocity of the rotation of the gas in the centre of the galaxy is low (~18 km s^{-1}, Hunter et al. 1998), suggesting a low escape velocity but the huge H I halo may prevent escape of the hot ejecta of the starburst region from the galaxy as a whole. The galaxy has both a high star formation rate (~0.2 M$_\odot$ yr^{-1}, Thronson et al. 1987) and supernova rate, contains numerous star clusters (~60, Gelatt, Hunter & Gallagher 2001) with the central one appearing to be young (~6–10 Myr, Böker et al. 2001) and a spherical distribution of older stars with a mean age of 3–5 Gyr (Bothun 1986). It has also been shown to contain molecular cloud complexes from CO observations (Hunter & Thronson 1996) and has an infrared luminosity (10–150 μm) of 3.7×10^{42} erg s^{-1} (Thronson et al. 1987, corrected for the distance assumed here – see below). The ionized gas it contains shows a very disturbed morphology and includes what appear to be many Hα bubbles, shells and filaments (Hunter & Gallagher 1990, 1997). The kinematics of the H II regions within the galaxy are very chaotic and could be the aftermath of a collision or merger (Hartmann, Geller & Huchra 1986). There is a gas-rich companion galaxy lying at a projected distance of ~40 kpc, coincident in projection with the outer edge of the extended H I halo, which could have been involved. Previous X-ray observations of this galaxy have detected the presence of discrete emission from point sources and diffuse emission from hot gas (Della Ceca, Griffiths & Heckman 1997; Vogler & Pietsch 1997).

The distance to NGC 4449 is not well established and ranges from 2.93 Mpc (Karachentsev & Drozdovsky 1998) to 5 Mpc (Aaronson & Mould 1983). We have chosen to adopt the lower value throughout this analysis as optical observations are showing objects within NGC 4449 to be resolved (Whiting 2002, private communication) suggesting a lower distance estimate to be more appropriate.

In Section 2 we describe the *Chandra* observation. The X-ray emission from the point sources is discussed in Section 3 and that from the diffuse emission is considered in Section 4. Section 5 contains a more general discussion of the relationship of the X-ray emission to that from other wavebands, the effects of the outflow of the X-ray emission on NGC 4449 and the morphology of the X-ray emission, whilst our main conclusions are summarized in Section 6.

2 OBSERVATIONS AND ANALYSIS

A 30-ks observation of NGC 4449 was obtained on 2001 February 4–5. Analysis was carried out on the data contained within the S3 chip of the ACIS-S instrument on board *Chandra* using CIAO (version 2.2.1), HEASOFT (version 5.1), XSPEC (version 11.1.0) and ASTERIX (version 2.3-b1). The data were reprocessed (CALDB version 2.9) and filtered to remove periods of flaring and lower than average count rates using the 3σ clipping technique of the lc_clean.sl script (available from the *Chandra* website). After these processes were

completed, a total of 22.12 ks of useful data remained. The data were then further filtered to contain data in the energy band from 0.3 to 8.0 keV (amounting to a total of ~22 300 counts on the S3 chip, of which ~10 700 come from within the D_{25} ellipse and of these ~6100 are due to diffuse emission) and were also background subtracted using the appropriately scaled CXC background event data set. (The one utilized for this observation had a total exposure of 137 391 s.) After production of an exposure map, the point sources present in the data were detected using the WAVDETECT tool, contained in the CIAO software, run with an exposure map, default wavelet scales of 2.0 and 4.0 pixels and a source significance threshold of 5×10^{-7}, a value of ~ (number of pixels)$^{-1}$, which should have limited the number of false detections to ~1. 32 point sources were detected and these are shown in Fig. 1 overlaid on a smoothed image of the S3 chip (smoothed with a Gaussian having a FWHM of 4 pixels, ~2 arcsec), while their positions and background-subtracted count rates are listed in Table 1. Of these 32 sources, eight do not lie within the optical extent of the galaxy, as measured by the D_{25} ellipse (de Vaucouleurs et al. 1991), also shown in Fig. 1. The 24 sources within the optical extent of the galaxy are those most likely to be associated with NGC 4449 and so are the only ones considered further in this analysis. In comparison, when the data were point source searched using CELLDETECT with an exposure map and default settings, only 18 sources were detected on the S3 chip. It was obvious from visual inspection of the data that several significant sources were missed by CELLDETECT. In addition on comparison with expected source counts from 'The *Chandra* Deep Field North Survey' (Brandt et al. 2001), we would expect ~16–20 background sources on the S3 chip at our level of completeness (see Section 3.1 for further details). For these reasons, we would expect more than the 18 sources detected by CELLDETECT and so the results from WAVDETECT have been adopted as being more reliable.

After detection, the point sources were subtracted from the data so that the diffuse X-ray emission contained within NGC 4449 could be investigated. The sources were simply blanked, using areas equivalent to the 3σ detection ellipses from WAVDETECT and allowance was made for the lost flux from these areas, which amounted to only 0.5 per cent of the total diffuse emission, in later analysis. Also, a three colour adaptively smoothed image of the galaxy has been produced using CSMOOTH in fast Fourier transform mode and this is shown in Fig. 2. The lower and upper sigmas for deriving the smoothing kernel were set at 2 and 5, respectively. This image shows that some of the sources are very soft and that the diffuse emission appears to consist of components of varying temperatures. The red, green and blue images used correspond to energy bands of 0.3–0.8, 0.8–2.0 and 2.0–8.0 keV, respectively. These bands were chosen so that the total number of counts in each band was approximately equal, thereby maximizing the signal-to-noise (S/N) ratio for the three bands and allowing point source searching of these individual bands to be performed most effectively. These bands are also in line with those used in the analysis of other starburst galaxies (e.g. NGC 253, Strickland et al. 2002). The diffuse emission is seen to be extended and the size of the region it occupies extends 2.4 kpc from NNE to SSW and 1.6 kpc from WNW to ESE down to a flux density of 1.3×10^{-13} erg s^{-1} cm^{-2} arcmin^{-2}.

The background-subtracted spectrum of the total X-ray emission from within the D_{25} ellipse of NGC 4449 was fitted using the modified Levenberg–Marquardt method and standard χ^2 statistic from XSPEC, with an absorbed two thermal component plus power-law fit. The resulting spectral fit is shown in Fig. 3. The absorbing column density was considered to be two components, one due to the interstellar medium (ISM) within the Milky Way (Galactic column
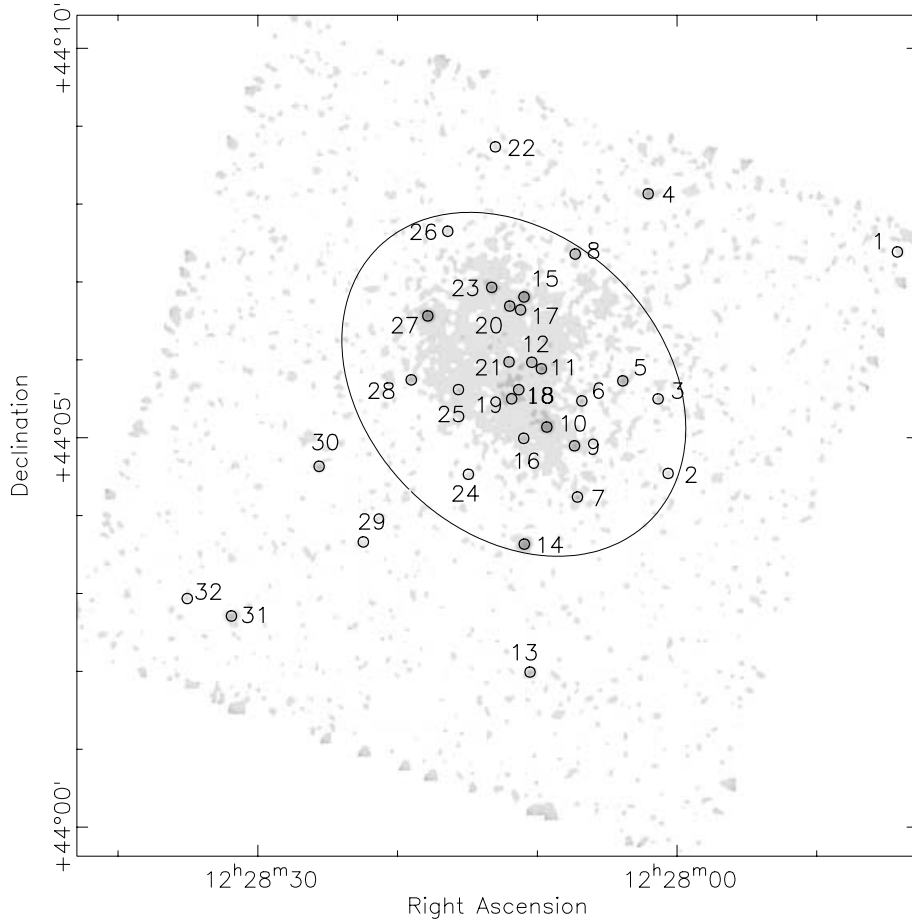
Figure 1. Low-resolution (smoothed using a Gaussian with FWHM of 4 pixels, ~2 arcsec), background-subtracted image of the S3 chip field of view marked with the 32 point sources listed in Table 1 and the D_{25} ellipse, representing the optical extent of NGC 4449. The extended diffuse emission associated with the galaxy is clearly visible.

density, $N_H = 1.4 \times 10^{20}$ cm^{-2}) and the other due to the ISM of NGC 4449. The two absorbed thermal components were modelled using the WABS (photoelectric absorption using Wisconsin cross-sections) and MEKAL thermal plasma codes within XSPEC, initially Galactic absorption and an abundance of 0.276 solar (the value obtained by Martin (1997) for NGC 4449) were assumed. Two thermal plasmas were used to represent the diffuse fraction of the total X-ray emission as images in the soft (0.3–0.8 keV) and medium (0.8–2.0 keV) energy bands, see Section 4, show different spatial distributions of the hot gas and also multiphase models are seen to be needed to best fit the emission from other starburst galaxies (e.g. NGC 253, Strickland et al. 2002; NGC 1569, Martin, Kobulnicky & Heckman 2002). A single-temperature fit to NGC 4449 also gave a less robust statistical fit and, in particular, when fitted to just the diffuse emission does not have a wide enough energy distribution to fit the spread seen in the data. The two-temperature model gives an absorption-corrected flux of $(2.39 \pm_{0.19}^{0.18}) \times 10^{-12}$ erg s^{-1} cm^{-2}, which corresponds to a total X-ray luminosity, in the 0.3–8.0 keV band, of $(2.46 \pm_{0.20}^{0.19}) \times 10^{39}$ erg s^{-1}. The fitted column density for NGC 4449 was $(1.31 \pm 0.52) \times 10^{21}$ cm^{-2}, with the two thermal components having temperatures of 0.27 ± 0.01 and 1.01 ± 0.06 keV and a fitted abundance of $0.29 \pm_{0.08}^{0.54}$ Z$_\odot$. The power-law component had a fitted photon index of $\Gamma = 2.05 \pm 0.46$. Of this total emission, ~60 per cent is from the resolved point sources, ~30 per

cent is from the cooler thermal component and ~10 per cent is from the hotter component.

3 POINT SOURCES

3.1 Source spectra

A background-subtracted spectrum was extracted for each of the 24 sources within the D_{25} ellipse. [The background spectra were taken from the aforementioned background file and were appropriately scaled. The use of the background files meant that the background spectrum was taken from the identical position on the charge-coupled device (CCD) and avoided the problem of contamination from adjacent sources.] The spectra were grouped so that each had a minimum of five data bins and when possible a minimum of 10 counts per bin. No attempt was made initially to fit the data where a source had less than 50 counts after background subtraction. The fits obtained for the five sources with the highest count rates are shown in Fig. 4. A comparison of the low count spectra with those fitted allowed a rough fit to be made to these sources individually by using the models of sources with similar spectra and hardness ratios (see below). The best fits obtained for the sources are summarized in Table 2. The same starting parameters were assumed for column densities and abundances as were used for fitting the total emission.

Table 1. Positions and count rates of the 32 sources detected in the NGC 4449 *Chandra* S3 chip data. Column 1 is the source number ordered in increasing RA. Columns 2 and 3 give the RA and Dec. of each source and Column 4 lists their background-subtracted count rates.

Source	RA (h m s)	Dec. (° ′ ″)	Count rate ($\times 10^{-3}$ count s^{-1})
1	12 27 44.24	44 07 23.0	0.13 ± 0.08
2	12 28 00.65	44 04 32.5	0.37 ± 0.14
3	12 28 01.36	44 05 29.9	0.63 ± 0.18
4	12 28 02.07	44 08 08.0	5.09 ± 0.48
5	12 28 03.89	44 05 43.8	5.36 ± 0.50
6	12 28 06.82	44 05 28.4	0.83 ± 0.21
7	12 28 07.13	44 04 14.4	0.96 ± 0.22
8	12 28 07.29	44 07 21.6	2.96 ± 0.37
9	12 28 07.34	44 04 53.8	5.65 ± 0.52
10	12 28 09.32	44 05 08.3	43.18 ± 1.42
11	12 28 09.71	44 05 53.1	7.53 ± 0.59
12	12 28 10.40	44 05 58.1	1.96 ± 0.32
13	12 28 10.52	44 01 59.5	1.04 ± 0.24
14	12 28 10.93	44 03 38.0	15.82 ± 0.87
15	12 28 10.95	44 06 48.5	38.60 ± 1.33
16	12 28 10.97	44 04 59.5	0.94 ± 0.23
17	12 28 11.20	44 06 38.5	4.13 ± 0.44
18	12 28 11.33	44 05 37.0	0.50 ± 0.19
19	12 28 11.84	44 05 30.0	1.80 ± 0.32
20	12 28 11.98	44 06 41.5	6.50 ± 0.56
21	12 28 12.02	44 05 58.4	2.18 ± 0.33
22	12 28 13.00	44 08 44.1	0.35 ± 0.13
23	12 28 13.26	44 06 55.8	9.61 ± 0.68
24	12 28 14.93	44 04 31.8	0.36 ± 0.14
25	12 28 15.64	44 05 37.1	0.63 ± 0.19
26	12 28 16.41	44 07 39.1	0.42 ± 0.14
27	12 28 17.83	44 06 33.9	51.35 ± 1.55
28	12 28 19.02	44 05 44.6	1.69 ± 0.28
29	12 28 22.44	44 03 39.7	0.39 ± 0.14
30	12 28 25.60	44 04 37.9	1.41 ± 0.26
31	12 28 31.86	44 02 42.5	1.74 ± 0.33
32	12 28 35.02	44 02 56.0	0.26 ± 0.12

For each of the individual source fits, the unabsorbed flux in the 0.3–8.0 keV energy band and luminosity (assuming a distance of 2.93 Mpc for NGC 4449) were calculated and these luminosities are also shown in Table 2 along with the errors determined from the 90 per cent confidence regions for the normalization of each model. In addition the data were point source searched in the three different energy bands used to produce the three colour image (soft 0.3–0.8 keV, medium 0.8–2.0 keV and hard 2.0–8.0 keV) so that hardness ratios for the individual sources within the D_{25} ellipse could be calculated for the sources detected in more than one of the energy bands. These ratios are shown in Table 3. The cumulative $\log(N)$–$\log(L_X)$ plot for the 24 fitted sources possibly associated with NGC 4449 is shown in Fig. 5. This has been fitted with a single power law with a slope of ~ -0.51 for the higher-luminosity sources. The highest-luminosity source is not included in the fit. To do so results in an offset between the data and the fitted line but does not alter the slope of the fit. The spectral fit to this source (source 28) does suggest it is a very unusual source as it is very soft, lies behind a high column density and has an extremely high luminosity ($>10^{41}$ erg s^{-1}). The fact that its spectrum contains <40 counts in total brings into question the robustness of the fit and for these reasons it has been excluded from the fit. Sources with luminosities below an absorption-corrected luminosity of 2.18×10^{37} erg s^{-1}, equivalent

to a flux of 2.12×10^{-14} erg s^{-1} cm^{-2}, were also not included in the fit and these figures represent the completeness limit for the data. The fitted value for the slope is comparable to the same fits for M82 and the Antennae where the slope was determined to be $\sim -0.45 \pm 0.06$ (Zezas et al. 2001). The absorption-corrected contribution to the X-ray luminosity of NGC 4449 from unresolved point sources is estimated to be $\sim(5.62 \pm^{6.08}_{4.30}) \times 10^{37}$ erg s^{-1}, equivalent to ~ 5 per cent of the diffuse emission (see Section 4).

Earlier *ROSAT* HRI observations of this galaxy (Vogler & Pietsch 1997) detected only seven point sources within the D_{25} ellipse. Of these seven, at least three of them have been resolved into more than one source using the superior arcsec spatial resolution of *Chandra* and an additional 13 sources have also been detected. The source identified as the supernova remnant (SNR), X4 in the *ROSAT* data corresponds to source 15 in our *Chandra* data when the source position is compared with the accurate position for the SNR obtained by Bignell & Seaquist (1983), from radio measurements and there are also two additional sources resolved at the position of X4 in the *ROSAT* data. This highlights the fact that luminosity estimates based on pre-*Chandra* data are affected by source confusion. Also of note is the fact that source 27 in our data (X7 in the *ROSAT* data) is much more luminous than it was in 1994 and now has the highest count rate for a single source in the galaxy rather than being fourth highest. See Table 4 for a comparison of the 0.1–2.4 keV absorption-corrected luminosities of sources that were both detected by *ROSAT* and not resolved into more than one source by *Chandra*.

In general, the sources seem to split into four classes, which can be represented by sources 14, 15, 27 and 2. Sources such as source 14 are very soft, luminous sources (supersoft sources, SSS), which show little emission above 1 keV. Source 15 is the SNR and at least five other sources show similar spectra and/or hardness ratios. Sources such as source 2 have spectra that contain hard emission up to ~ 5 keV and sources in this group seem to be best fitted by power-law models. They are generally fitted with a higher column density and lower photon index than other sources and may be background active galactic nuclei (AGN). Sources such as source 27 also have harder components to their spectra, showing emission above 5 keV and are fitted by power laws with $1.3 \leqslant \Gamma \leqslant 3.0$, typical of X-ray binaries (XRB). See Section 3.2 below for further discussion of the brightest sources. Fig. 6 shows a comparison of the hard and soft hardness ratios for the sources detected in all three energy bands. The hard ratio is $(h - m)/(h + m)$, while the soft ratio is $(m - s)/(m + s)$, where s is the count rate in the soft band (0.3–0.8 keV), m is the count rate in the medium band (0.8–2.0 keV) and h is the count rate in the hard band (2.0–8.0 keV). The sources represented by squares were only detected in two of the three energy bands and so their positions represent the most extreme positions possible for them on this plot. Those at the bottom need to move vertically upwards while those to the right will need to move horizontally to the left. The sources appear to clump in groups on this plot with the SNR and SSS sources being softer than those we have classified as XRB and AGN. The right-hand plot in this figure shows some theoretical tracks of how the position of a source would vary depending on which type of spectral model is assumed for it, what value the absorbing column density that it lies behind has and what temperature or photon index is assumed for the model, for comparison with the plotted source positions. An attempt has been made to classify the sources using the shape and range of spectra and their positions on the hardness ratio plot. The suggested classifications are shown in column 8 of Table 2. The D_{25} ellipse covers ~ 25 per cent of the S3 chip and as such it would be expected from the background number
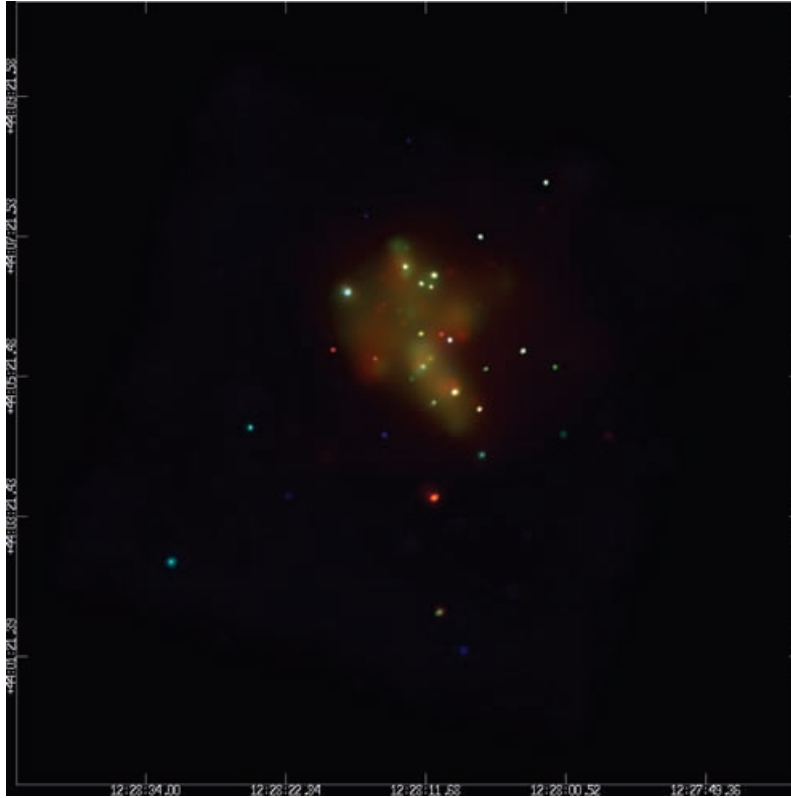
Figure 2. Adaptively smoothed three-colour image of NGC 4449 (red, 0.3–0.8 keV; green, 0.8–2.0 keV; blue, 2.0–8.0 keV). The extent of the diffuse emission is ∼2.4 kpc from NNE to SSW and ∼1.6 kpc from WNW to ESE. The variation of hardness in the spectra of the resolved sources is evident from their varying colours and is indicative of the presence of different types of sources, such as XRBs, SNRs and SSS.
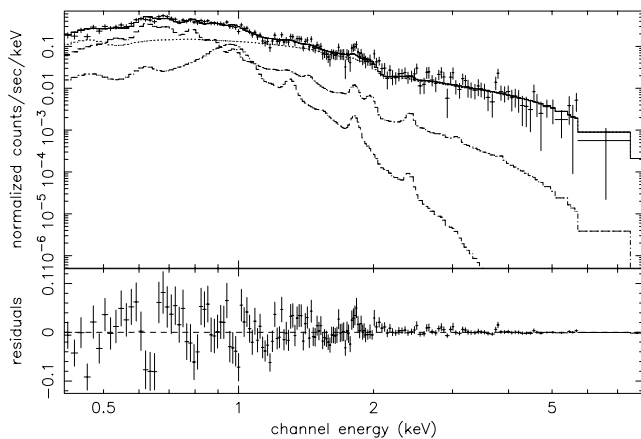

Figure 3. Fitted spectrum of the total X-ray emission from NGC 4449. The fit shown is an absorbed two-temperature plus power-law fit, with a column density of $N_H = 1.40 \times 10^{20}$ cm^{-2} assumed for Galactic absorption and a fitted column density of $N_H = (1.31 \pm 0.52) \times 10^{21}$ cm^{-2} for the absorption within NGC 4449. The fitted temperatures of the two thermal components are 0.27 ± 0.01 and 1.01 ± 0.06 keV with the fitted abundance for both components being $0.29^{+0.54}_{-0.08}$ Z$_\odot$ and the fitted photon index of the power-law component having a value of $\Gamma = 2.05 \pm 0.46$. The individual contributions of the separate components of the fit are also included.

counts quoted in Section 2 that ∼4–5 background sources should be found within this area. This figure agrees well with the number of sources classified as potential background AGN. In contrast to this, the eight point sources detected outside the D_{25} ellipse are only

about a half to two-thirds of what would be expected, suggesting that our completeness level estimate may be at slightly too low a flux.

3.2 More detail on the brightest sources

3.2.1 Source 10: SNR?

This source lies in the soft region of the hardness plot of Fig. 6 to the left of the area occupied by the known SNR. It is best fitted by an absorbed thermal bremsstrahlung model. Its position would also suggest it should have a low column density as it lies to the left of the theoretical tracks. This does not appear to be the case and fitting with other models gives an even higher column density for a power-law model or unphysical results. This source was also detected (source X7) in the earlier *ROSAT* observations and shows no evidence for variability as seen in Table 4. Hence, it seems more likely that it is a SNR than an XRB.

3.2.2 Source 14: SSS

This source is very soft and it can be fitted in a similar way to CAL 87 (Ebisawa et al. 2001) using an absorbed blackbody component and several absorption edges, indicative of a white dwarf binary system. For such a fit, three absorption edges are included at energies of 0.40, 0.59 and 0.85 keV, the value of N_H increases to 3.24×10^{21} cm^{-2} and kT decreases to 0.065 keV, compared with the one-component fit shown in Table 2, while the absorption-corrected luminosity in the 0.3–8.0 keV band increases to ∼4.05×10^{39} erg s^{-1}. The absorption edges are possibly connected with the presence
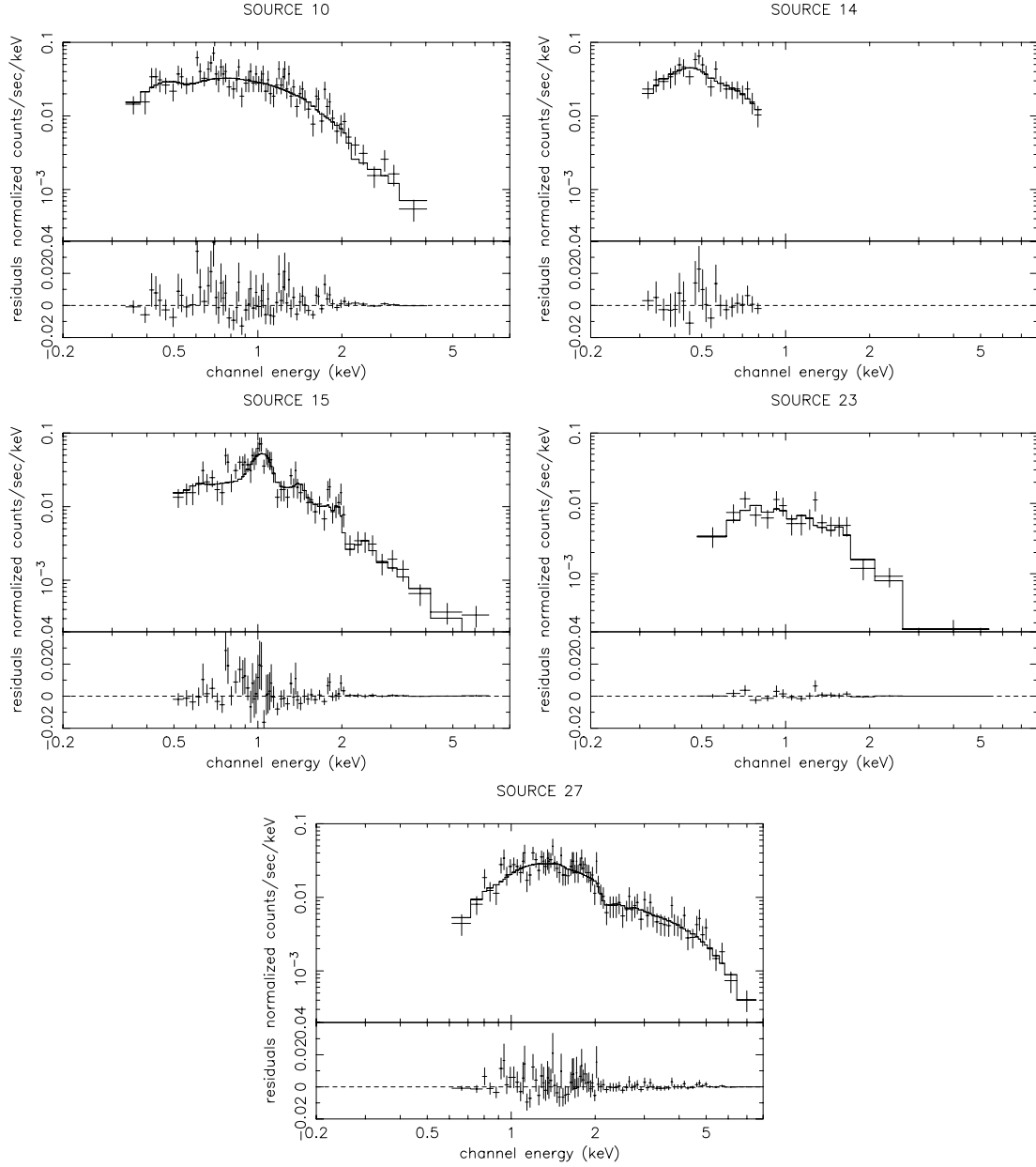
Figure 4. Spectra and best-fitting models for the brightest sources detected within the D_{25} ellipse. Results are shown for source 10 (top left), source 14 (top right), source 15 (middle left), source 23 (middle right) and source 27 (bottom). All the fits are for the absorbed one-component models shown in Table 2. More detailed fits for the brighter sources are discussed in Section 3.2.

of the following elements: 0.40 keV, N VI or C VI; 0.59 keV, O VII or N VII; 0.85 keV, O VIII and/or O VII (the low source counts making a definite identification difficult). The blackbody temperature fitted here lies in the range $T \sim 60$–80 eV, where both O VII and O VIII edges would be expected to be present with the latter being more abundant (Ebisawa et al. 2001). This source has a greatly increased absorption-corrected luminosity compared with the earlier *ROSAT* observations; however, the difference is in part due to the different spectral models used to fit the spectrum. The improved spectral resolution of *Chandra* compared with *ROSAT* clearly shows that a 5-keV thermal bremsstrahlung model is inappropriate for this source, as all of its emission lies below 1 keV. In Table 4, the absorption-corrected luminosity is also much higher than that shown

in Table 2 and quoted above due to the value in Table 4 including emission down to 0.1 keV rather than 0.3 keV. These facts make it difficult to assess whether there has been any intrinsic increase in the sources luminosity over the last decade. When the *Chandra* data are fitted with the 5-keV thermal bremsstrahlung model there is agreement with the *ROSAT* HRI data, within errors.

3.2.3 Source 15: SNR

This source has been identified as a young and very luminous SNR embedded in an H II region from observations in several different wavebands: radio (Seaquist & Bignell 1978), optical (Balick & Heckman 1978; Blair, Kirshner & Winkler 1983), ultraviolet (Blair

Table 2. Best-fitting single-component models for the spectra of the 24 point sources. Column 1 gives the source numbers as shown in Fig. 1. Column 2 contains the best-fitting absorbed single-component models obtained. In each case, the absorbing column due to the Milky Way, wabs$_{\rm Gal}$ is assumed to be $N_{\rm H}$ = 1.4×10^{20} cm^{-2}. Column 3 is the column density obtained from fitting the wabs (photoelectric absorption using Wisconsin cross-sections) component, column 4 is the fitted temperature for the mekal, brems (thermal bremsstrahlung), bb (blackbody) and nei (non-equilibrium ionization) models for the thermal components, column 5 is the photon index for the po (power-law) models, column 6 the statistic of each fit and column 7 the absorption-corrected luminosity for each source. The errors shown on the luminosities are from the 90 per cent confidence regions (1.64σ) for the normalization of each model. Where only one value is shown this is an upper limit from the same 90 per cent confidence regions. Column 8 lists the type of source each object might be from comparison with the spectra and hardness ratios of the identified sources within the galaxy.

Source	Model	$N_{\rm H}$ (cm^{-2})	kT (keV)	Γ	χ^2/d.o.f.	Luminosity (erg s^{-1})	Source type
2	wabs$_{\rm Gal}$(wabs(po))	3.14×10^{21}		0.61	1.78/5	$(7.10 \pm^{7.31}) \times 10^{36}$	AGN
3	wabs$_{\rm Gal}$(wabs(mekal))	3.68×10^{21}	0.90		0.49/2	$(5.87 \pm^{2.86}_{2.87}) \times 10^{36}$	SNR/XRB
5	wabs$_{\rm Gal}$(wabs(po))	6.58×10^{20}		1.30	1.39/8	$(5.15 \pm^{0.75}_{0.92}) \times 10^{37}$	XRB
6	wabs$_{\rm Gal}$(wabs(mekal))	1.31×10^{21}	0.82		2.01/2	$(5.51 \pm^{3.52}) \times 10^{36}$	SNR/XRB
7	wabs$_{\rm Gal}$(wabs(po))	1.39×10^{21}		0.40	1.00/2	$(2.18 \pm^{0.98}) \times 10^{37}$	AGN
8	wabs$_{\rm Gal}$(wabs(po))	1.53×10^{20}		1.33	0.38/3	$(2.59 \pm^{2.14}_{0.69}) \times 10^{37}$	XRB
9	wabs$_{\rm Gal}$(wabs(po))	3.93×10^{20}		2.88	7.87/8	$(2.94 \pm^{0.66}_{0.56}) \times 10^{37}$	SNR/XRB
10	wabs$_{\rm Gal}$(wabs(brems))	9.29×10^{20}	1.42		83.37/69	$(2.24 \pm^{0.12}_{0.12}) \times 10^{38}$	SNR/XRB
11	wabs$_{\rm Gal}$(wabs(po))	3.50×10^{21}		1.64	9.07/13	$(8.91 \pm^{1.23}_{1.24}) \times 10^{37}$	XRB
12	wabs$_{\rm Gal}$(wabs(bb))	4.15×10^{20}	0.091		4.46/4	$(1.28 \pm^{2.11}) \times 10^{37}$	SSS
14	wabs$_{\rm Gal}$(wabs(bb))	8.96×10^{20}	0.097		12.44/20	$(1.24 \pm^{0.12}_{0.11}) \times 10^{38}$	SSS
15	wabs$_{\rm Gal}$(wabs(nei))	1.26×10^{21}	2.58		65.50/60	$(2.34 \pm^{0.14}_{0.13}) \times 10^{38}$	SNR
16	wabs$_{\rm Gal}$(wabs(po))	1.40×10^{22}		2.53	0.90/3	$(3.14 \pm^{1.16}_{1.23}) \times 10^{37}$	XRB
17	wabs$_{\rm Gal}$(wabs(nei))	7.45×10^{20}	19.21		5.33/5	$(2.51 \pm^{0.50}_{0.49}) \times 10^{37}$	SNR/XRB
18	wabs$_{\rm Gal}$(wabs(nei))	3.82×10^{20}	3.05		1.03/3	$(3.02 \pm^{1.37}) \times 10^{36}$	SNR/XRB
19	wabs$_{\rm Gal}$(wabs(po))	1.31×10^{21}		1.35	0.47/3	$(2.33 \pm^{1.55}_{0.71}) \times 10^{37}$	XRB
20	wabs$_{\rm Gal}$(wabs(po))	3.45×10^{21}		2.76	8.20/10	$(7.43 \pm^{1.04}_{1.23}) \times 10^{37}$	SNR
21	wabs$_{\rm Gal}$(wabs(bb))	2.45×10^{21}	0.080		1.71/2	$(7.19 \pm^{1.07}_{2.76}) \times 10^{37}$	SNR/SSS
23	wabs$_{\rm Gal}$(wabs(nei))	9.00×10^{21}	1.30		12.07/16	$(8.06 \pm^{0.98}_{1.01}) \times 10^{38}$	SNR/XRB
24	wabs$_{\rm Gal}$(wabs(po))	1.10×10^{22}		0.97	2.25/6	$(5.79 \pm^{5.22}) \times 10^{36}$	AGN
25	wabs$_{\rm Gal}$(wabs(bb))	1.11×10^{21}	0.130		0.62/2	$(5.17 \pm^{107.71}) \times 10^{36}$	SSS/XRB
26	wabs$_{\rm Gal}$(wabs(brems))	4.72×10^{21}	54.85		0.74/2	$(4.99 \pm^{3.57}) \times 10^{36}$	AGN
27	wabs$_{\rm Gal}$(wabs(po))	6.49×10^{21}		1.91	64.38/86	$(8.19 \pm^{0.42}_{0.41}) \times 10^{38}$	XRB
28	wabs$_{\rm Gal}$(wabs(bb))	5.01×10^{21}	0.050		1.28/3	$(4.27 \pm^{1.32}_{1.34}) \times 10^{41}$	SSS

et al. 1984) and X-ray (Blair et al. 1983; Vogler & Pietsch 1997). Fitting this source with an absorbed, non-equilibrium ionization model (as used for modelling other SNR, e.g. Yokogawa et al. 2002) gives an X-ray temperature, $T_{\rm X} \sim 2.2 \times 10^7$ K, a column density of $N_{\rm H} = 1.26 \times 10^{21}$ cm^{-2} and an absorption-corrected luminosity of $L_{\rm X} = (2.34 \pm^{0.14}_{0.13}) \times 10^{38}$ erg s^{-1} in the 0.3–8.0 keV energy band, which are comparable to the values recently obtained for the same SNR Patnaude & Fesen (2003). (After allowing for differences in assumed distance, they quote a luminosity of $L_{\rm X} = 1.4 \times 10^{38}$ erg s^{-1} in the 0.5–2.1 keV energy band, a temperature of $T \sim 9.2 \times 10^6$ K and an absorbing column density of $N_{\rm H} = 1.7 \times 10^{21}$ cm^{-2}.) Following the same analysis that Blair et al. (1983) performed on this SNR, we find first that our fitted temperature is higher than the 6×10^6 K assumed by Blair et al. (1983, which came from the average temperature determined from *Einstein* SSS observations of young SNR). This higher temperature leads to an age for the SNR of $\sim$270 yr and a density of 120–200 cm^{-3} for the medium into which the SN exploded. These results are higher than the age of $\sim$120 yr and density of $\sim$25 cm^{-3} reported by Blair et al. (1983). Allowing for the difference in assumed distances to NGC 4449 would increase our age estimate to $\sim$380 yr without affecting the density. Compared

with the non-equilibrium ionization fit for the ionization time-scale, where $\tau = nt = 4.96 \times 10^{11}$ cm^{-3} s, with the 90 per cent confidence regions for this parameter giving a range of $3.61 \times 10^{11} \leqslant \tau \leqslant 5.00 \times 10^{13}$ cm^{-3} s, the product of our calculated values gives $1.0 \times 10^{12} \leqslant \tau \leqslant 1.7 \times 10^{12}$ cm^{-3} s, which gives reasonable agreement for the two methods.

3.2.4 Source 23: XRB?

The position of this source on the hardness plot of Fig. 6 places it in the group of XRBs; however, its spectrum is best fitted by an absorbed non-equilibrium ionization model and this source shows no strong evidence for variability over the past 10 yr, factors which may be more indicative of a SNR than XRB.

3.2.5 Source 27: XRB

This source is now the source with the highest individual count rate in NGC 4449. Its luminosity has increased by nearly an order of magnitude since the *ROSAT* HRI observations of this galaxy in 1994, reported by Vogler & Pietsch (1997, see Table 4 for comparative

Table 3. Hardness ratios, where possible, for the 24 sources detected within the D_{25} ellipse. Soft band, *s*, 0.3–0.8 keV, medium band, *m*, 0.8–2.0 keV and hard band, *h*, 2.0–8.0 keV. Where no counts are shown, WAVDETECT failed to detect the object in that energy band. Column 1 gives the source numbers as shown in Fig. 1. Columns 2–4 are the counts in the three different energy bands and columns 5 and 6 give the values of the hardness ratios calculated as detailed in the column headings.

| Source	Counts in Soft band	Counts in Medium band	Counts in Hard band	$\frac{(m-s)}{(m+s)}$	$\frac{(h-m)}{(h+m)}$
2	–	2.0 ± 1.4	3.9 ± 2.0	–	0.32 ± 0.43
3	–	8.9 ± 8.0	–	–	–
5	25.7 ± 5.1	58.7 ± 7.7	34.7 ± 5.9	0.39 ± 0.12	-0.26 ± 0.11
6	–	8.9 ± 8.0	–	–	–
7	–	3.9 ± 2.0	7.9 ± 2.8	–	0.34 ± 0.31
8	12.8 ± 3.6	31.8 ± 5.7	20.8 ± 4.6	0.43 ± 0.17	-0.21 ± 0.14
9	55.2 ± 7.5	57.4 ± 7.6	6.9 ± 2.6	0.02 ± 0.10	-0.79 ± 0.16
10	533.7 ± 23.2	336.9 ± 18.4	93.6 ± 10.0	-0.23 ± 0.03	-0.57 ± 0.06
11	23.9 ± 5.0	88.0 ± 9.4	54.6 ± 7.4	0.57 ± 0.11	-0.23 ± 0.09
12	39.6 ± 6.4	–	–	–	–
14	349.0 ± 18.7	7.9 ± 2.8	–	-0.96 ± 0.07	–
15	141.7 ± 12.0	590.5 ± 24.4	126.5 ± 11.3	0.61 ± 0.04	-0.64 ± 0.11
16	–	10.5 ± 3.3	6.9 ± 2.6	–	-0.21 ± 0.17
17	30.1 ± 5.6	54.1 ± 7.4	–	0.29 ± 0.49	–
18	–	–	–	–	–
19	–	22.4 ± 4.9	14.7 ± 3.9	–	-0.21 ± 0.17
20	30.1 ± 5.6	91.1 ± 9.6	19.7 ± 4.5	0.50 ± 0.10	-0.64 ± 0.11
21	14.8 ± 4.0	31.7 ± 5.7	–	0.36 ± 0.16	–
23	51.8 ± 7.3	129.6 ± 11.4	27.6 ± 5.3	0.43 ± 0.09	-0.65 ± 0.09
24	–	–	4.9 ± 2.2	–	–
25	–	–	–	–	–
26	–	–	4.9 ± 2.2	–	–
27	32.4 ± 5.7	669.5 ± 25.9	448.7 ± 21.2	0.91 ± 0.05	-0.20 ± 0.03
28	36.6 ± 6.1	–	–	–	–
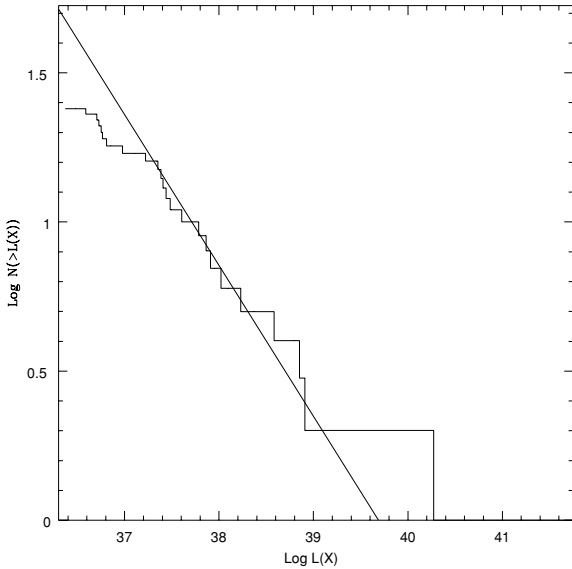
Figure 5. Log(N)–log (L_X) plot for the 24 fitted resolved point sources lying within the D_{25} ellipse. The line shown is the power-law fit to the high-luminosity end of the data. The slope of this fit is -0.51 and incompleteness occurs at an absorption-corrected luminosity of 2.18×10^{37} erg s^{-1}, which corresponds to a limiting absorption-corrected flux of 2.12×10^{-14} erg s^{-1} cm^{-2}.

figures). This is confirmed by the results obtained by fitting it with a 5-keV thermal bremsstrahlung model, as used for the *ROSAT* data, where its luminosity is seen to have increased by a factor of at least 3. Its high luminosity and apparent long-term variability would suggest that it is a high-mass X-ray binary (HMXB). The light curve shows no sign of variability within our 30-ks observation.

4 DIFFUSE EMISSION

A point source and background-subtracted spectrum of the diffuse emission within the D_{25} ellipse was extracted and this is shown in Fig. 7. The fitted model shown is an absorbed two-temperature fit, wabs$_{Gal}$[wabs(mekal+mekal)]. The component due to Galactic absorption (wabs$_{Gal}$) has its absorption column density fixed at $N_H = 1.4 \times 10^{20}$ cm^{-2} and the fit gives $N_H = (1.29 \pm 0.38) \times 10^{21}$ cm^{-2} for the absorbing column local to NGC 4449 and values of kT of 0.28 ± 0.01 and 0.86 ± 0.04 keV for the soft and medium thermal components, respectively. The fitted abundance for the two thermal components is 0.32 ± 0.08 Z$_\odot$. The total absorption-corrected flux in the 0.3–8.0 keV energy band for the diffuse emission is $(8.86 \pm^{0.61}_{0.60}) \times 10^{-13}$ erg s^{-1} cm^{-2}, which corresponds to an absorption-corrected luminosity of $(9.14 \pm^{0.63}_{0.62}) \times 10^{38}$ erg s^{-1}. Of this total emission, 75 per cent is in the soft component and 25 per cent is in the medium component and allowance has been made for the flux lost during the point source subtraction. The errors shown here are based on the 90 per cent confidence levels $(1.64\,\sigma)$ for the normalization values obtained from the fit. Adding a power-law component to allow for unresolved point sources within the diffuse emission neither improves the fit significantly nor alters the fitted parameters for the thermal components. The photon index resulting from such a fit was $\Gamma = 2.53$ and the fractional split of the flux between the three components was: soft ~70 per cent; medium ~25 per cent; power law ~5 per cent.

Other parameters of the two gas components have been calculated and these are shown in Table 5. The assumptions of spherical

Table 4. Comparison of the absorption-corrected luminosities for sources 10, 14, 23 and 27 obtained from *ROSAT* PSPC observations (11/1991), *ROSAT* HRI observations (12/1994) and *Chandra* ACIS-S observations (02/2001). The *ROSAT* values are from Vogler & Pietsch (1997) and are for 5-keV thermal bremsstrahlung spectra, corrected for Galactic absorption. The first column of *Chandra* values are for the best fits discussed in the text, corrected for Galactic absorption. All luminosities are for the 0.1–2.4 keV energy band and the *Chandra* values have been scaled to account for the differences in assumed distances to NGC 4449. The errors shown on the *Chandra* data are from the 90 per cent confidence levels (1.64σ) of the normalizations of the fits. Columns 1 and 2 are the source numbers allocated in the respective data sets and columns 3–5 give the absorption-corrected luminosities fitted to the three data sets. Column 6 shows the absorption-corrected luminosities obtained for the *Chandra* data when they are fitted with a 5-keV thermal bremsstrahlung model, corrected for Galactic absorption.

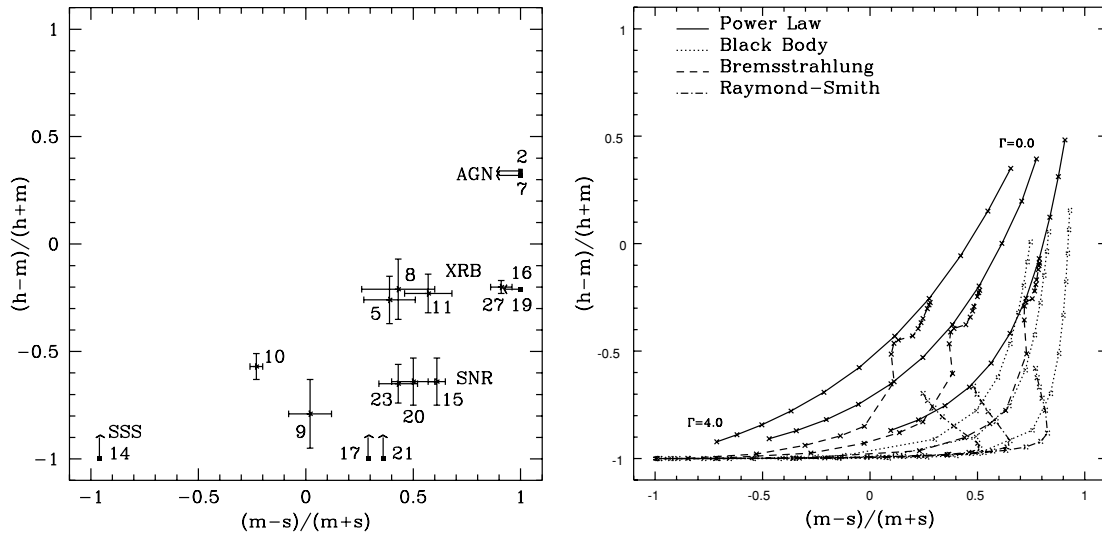| *Chandra*	*ROSAT*	L_X(PSPC) ($\times 10^{38}$ erg s^{-1})	L_X(HRI) ($\times 10^{38}$ erg s^{-1})	L_X(ACIS-S) ($\times 10^{38}$ erg s^{-1})	L_X(ACIS-S 5 keV) ($\times 10^{38}$ erg s^{-1})
10	X1	2.92 ± 0.43	3.10 ± 0.37	$3.24^{0.18}_{0.18}$	$2.58^{0.15}_{0.15}$
14	X3	0.70 ± 0.23	1.67 ± 0.27	$105.45^{9.53}_{10.18}$	$1.82^{0.20}_{0.21}$
23	X6	0.84 ± 0.28	0.76 ± 0.21	$14.60^{1.87}_{1.68}$	$1.01^{0.12}_{0.13}$
27	X7	1.88 ± 0.37	1.00 ± 0.21	$7.33^{0.38}_{0.36}$	$6.18^{0.33}_{0.33}$

Figure 6. Left: hard versus soft hardness ratios for the sources detected in the separate energy bands. The hard hardness ratio is calculated from the 2.0–8.0 and 0.8–2.0 keV energy bands and the soft hardness ratio is calculated from the 0.8–2.0 and 0.3–0.8 keV energy bands in the usual way as defined in the headings of columns 5 and 6 of Table 3. An indication of the likely origin of the sources depending on the location in this plot is also shown by the labels placed next to known sources. Right: theoretical tracks showing the positions different sources would occupy on the hardness ratio plot. The three lines of each type have column densities of 1.4×10^{20} cm^{-2} (Galactic N_H), 1.0×10^{21} cm^{-2} (fitted column density for the total emission from NGC 4449) and 3.0×10^{21} cm^{-2} (average fitted column density for the fitted sources on the hardness ratio plot), respectively, moving from left to right across the plot. For the three thermal models, the temperatures increase from bottom left to top right. Blackbody, kT ranges from 0.04 to 1.0 keV; bremsstrahlung, kT ranges from 0.2 to 100 keV; Raymond–Smith, kT ranges from 0.1 to 2.0 keV and the plots shown are for solar abundance. Decreasing the abundance moves the Raymond–Smith tracks to the left.

symmetry and a filling factor of 1 are both likely to be overestimates, particularly in the case of the medium emission (see below), resulting in the figures being underestimates for n_e and P and overestimates for M, E_{th} and t_{cool} (see Strickland & Stevens 2000 for a discussion of filling factors and their likely values in galactic winds). These parameters will be discussed further in Section 5.2.

In a further attempt to look at the abundances within the thermal components and, in particular, the ratio of α-elements to Fe the spectrum was refitted using variable abundance mekal models for the two thermal components. The abundances of the two thermal components were tied and the individual abundances of Mg, Ne, Si and Ca relative to solar values were tied to that of O to form the group of α-elements. The fitted abundances for the α-elements

and Fe were $0.27^{0.01}_{0.03}$ and $0.30^{0.02}_{0.02}$ Z$_\odot$, respectively, with a χ^2/d.o.f. of 201/117. The α/Fe ratio obtained from these values is not significantly different from solar ($0.91^{0.07}_{0.10}$ Z$_\odot$) in contrast to the values of Martin et al. (2002) for the dwarf starburst NGC 1569, where values of 2.1–3.9 Z$_\odot$ are quoted. The difference in these values could reflect different contributions made to the hot gas from SNe. Type II SNe are the sources of α-elements while Fe is produced from type I SNe. The higher values for the α/Fe ratio for NGC 1569 would therefore suggest the presence of more type II SNe than in NGC 4449 and could suggest that NGC 1569 is experiencing shorter more intense bursts of star formation than NGC 4449. In the latter case, as discussed by Della Ceca et al. (1997), the star formation and energy injection from star-forming regions may be more continuous as it is not clear that the present star formation rate is much larger
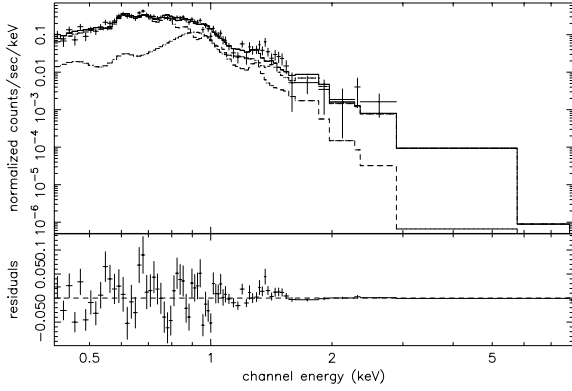
Figure 7. Fitted spectrum of the NGC 4449 diffuse emission. The fit shown is an absorbed two-temperature fit, with a column density of $N_H = 1.4 \times 10^{20}$ cm^{-2} assumed for Galactic absorption and fitted values of $N_H = (1.29 \pm 0.38) \times 10^{21}$ cm^{-2} for the absorption within NGC 4449 and temperatures of 0.28 ± 0.01 and 0.86 ± 0.04 keV for the two thermal components. The fitted abundance for the two thermal components was found to be (0.32 ± 0.08) Z$_\odot$.

Table 5. Parameters for the two gas components of the diffuse emission. Assumptions: $V = 6 \times 10^{65}$ cm^3 (assumes spherical symmetry); $D = 2.93$ Mpc; filling factor, $f = 1$; $n_e \sim (EI/Vf)^{1/2}$, where EI is the emission integral (norm$\times 4\pi D^2)/10^{-14}$ and norm is the normalization obtained from the spectral fitting; $P \sim 2n_e\,kT$, $M \sim n_e\,m_p\,Vf$, $E_{th} \sim 3n_e kTV$ and $t_{cool} \sim (3kT)/(\Lambda n_e)$, where $\Lambda = L_X/EI$.

Emission	Soft	Medium
kT (keV)	0.28 ± 0.01	0.86 ± 0.04
T (K)	$(3.24 \pm 0.12) \times 10^6$	$(9.97 \pm 0.46) \times 10^6$
L_X(erg s^{-1})	$(6.83^{0.35}_{0.36}) \times 10^{38}$	$(2.26^{0.27}_{0.26}) \times 10^{38}$
n_e(cm^{-3})	$0.0122^{0.0003}_{0.0003}$	$0.0059^{0.0004}_{0.0003}$
E_{th}(erg)	$(9.66^{0.43}_{0.43}) \times 10^{54}$	$(1.49^{0.12}_{0.10}) \times 10^{55}$
M(M$_\odot$)	$(6.02^{0.15}_{0.15}) \times 10^6$	$(3.01^{0.20}_{0.15}) \times 10^6$
P(dyn cm^{-2})	$(1.07^{0.05}_{0.05}) \times 10^{-11}$	$(1.65^{0.14}_{0.11}) \times 10^{-11}$
t_{cool}(yr)	$(4.66^{0.40}_{0.41}) \times 10^8$	$(2.02^{0.39}_{0.36}) \times 10^9$

than that in the past on average and as such the longer time periods involved will reflect a larger contribution from type I SNe.

In order to look for variations in temperature within the diffuse emission, the region it occupies was divided into nine regions and the spectra for each region was extracted and fitted. The regions are shown overlaid on the smoothed (using a Gaussian with FWHM of 4 pixels $\sim$2 arcsec) point source and background-subtracted image of NGC 4449 in Fig. 8 and the resulting spectral fits are shown in Table 6. Where possible, a two-temperature fit was used, but for the four regions with the lowest number of counts (1, 2, 3 and 7) this was not possible. Either the fitted temperatures of the two components were the same, within errors, or the normalization for one of the components went to zero. For these four regions, the results of single-temperature fits are given. In addition, for each region, the $(m-s)/(m+s)$ hardness ratio has been calculated to further highlight variations within the galaxy and these are shown in Table 7. To make a comparison of the results contained in Tables 6 and 7 clearer, colour-coded maps of the temperatures, column densities and hardness ratios are shown in Fig. 9. The two upper panels compare the fitted temperatures for the nine regions. The one on the left shows the temperatures of the softer thermal components, where

two temperatures were fitted and the right-hand panel shows the temperatures of the harder components. Where only one temperature was fitted, this is shown in both panels. The lower left-hand panel compares the column densities [log(N_H)] fitted to the nine regions, while the lower right-hand one shows how the $(m-s)/(m+s)$ hardness ratio varies.

These results are not very conclusive but do suggest a reduced column density in a region running from north to south across the centre of the galaxy and also across the northern edge and into the northeast of the galaxy. The temperature of the softer thermal components seem to be highest in the north of the galaxy and in an arc running south across the centre of the galaxy and into the southeast. The hardness ratios suggest that generally, the emission is slightly higher in the 0.3–0.8 keV energy band than in the 0.8–2.0 keV band. Looking at the soft, medium and hard energy band images (0.3–0.8, 0.8–2.0 and 2.0–8.0 keV, respectively), a difference can be seen between the spatial distribution of the extended diffuse emission in these three bands (Fig. 10). These bands were originally chosen to have roughly equal counts in the three bands and they highlight the relative contributions made by the diffuse emission and point sources to the different bands. Surprisingly, the 0.3–0.8 keV band image shows the diffuse emission to be extending to the west of the galaxy into regions where the spectral fits gave some of the highest column densities. Such high absorption should reduce the soft thermal emission and suggests that the single-temperature fits in these regions are not the best models. It is worth noting here that when two-temperature models were fitted to regions 1, 2 and 3, lower column densities were obtained but none of the results were well constrained.

To obtain a clearer picture of the distribution of peaks in the X-ray emission, surface brightness slices were taken across the galaxy in four directions (N to S, NW to SE, W to E and SW to NE), centred on the trough of the X-ray emission in the centre of the galaxy at $\alpha = 12^h28^m11^s.7$, $\delta = +44°06'04''.6$ with a length of 200 arcsec and a width of 20 arcsec. The positions of these slices are overlaid on the Hα image of NGC 4449 (kindly supplied by Deidre A. Hunter) shown in Fig. 11. In addition surface brightness profiles were also taken from the Hα image using the same slices. The resulting profiles from these slices are shown in Fig. 12, with those from the diffuse X-ray emission, shown by the crosses and dashed curves, overlaid on those from the Hα emission (solid curves). Although the X-ray data has been point source subtracted, the Hα data has not. There is very little correlation between the positions of the resolved X-ray point sources and the numerous H II regions seen in the Hα data and so the slices are being used to look for association of the diffuse X-ray emission with the star-forming regions (see Section 5.1.2 for further discussion).

5 DISCUSSION

It is apparent from Fig. 10 that the hardest ($>$2 keV) fraction of the diffuse emission is confined to the central region of the galaxy along a ridge running from NNE to the centre. This is in the same direction as the orientation of the major axis of the galaxy. The medium (0.8–2.0 keV) diffuse emission is less extended than the soft ($<$0.8 keV) emission with the most intense regions of emission in both of these bands being coincident with the regions where the highest density of star clusters is seen (as identified by Gelatt et al. 2001), suggesting that this emission is associated with the increased star formation occurring in these regions. The less intense bulging of the emission seen to the ESE and WNW could be indicative of a bipolar outflow along the minor axis of the galaxy as would be
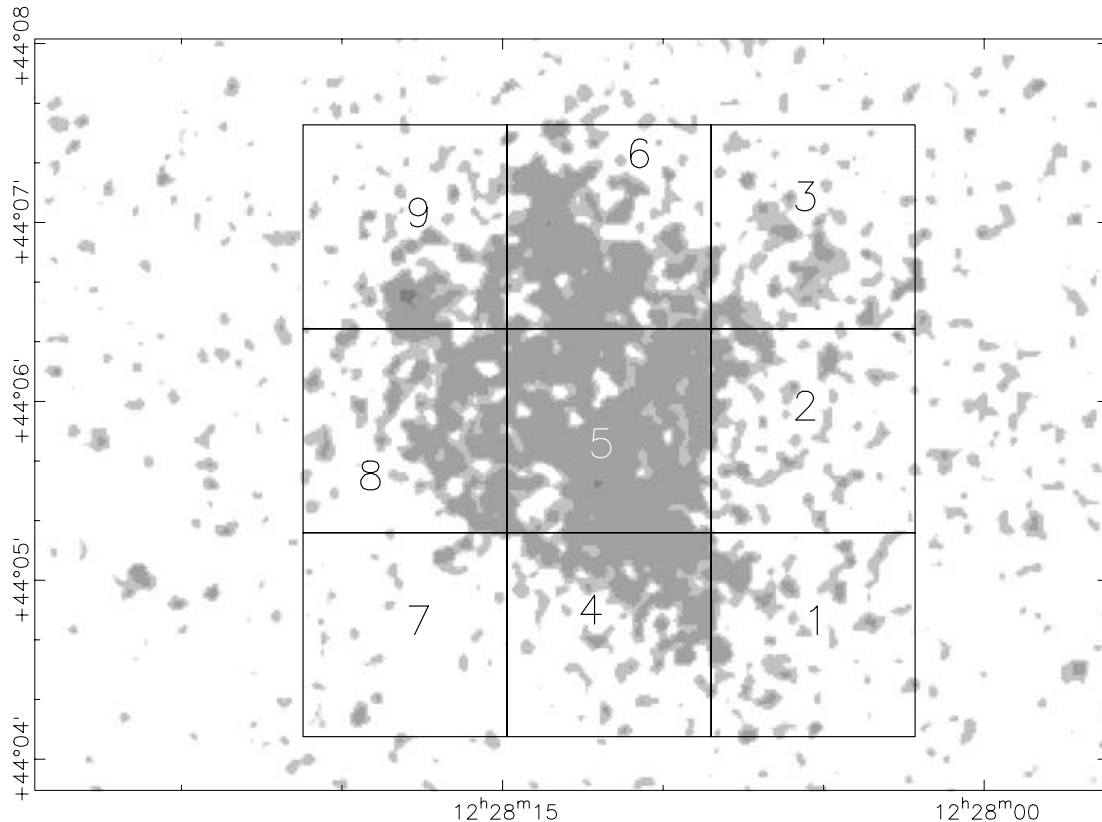
Figure 8. Low-resolution (smoothed using a Gaussian with FWHM of 4 pixels, ∼2 arcsec) image of the point source and background-subtracted diffuse X-ray emission overlaid with the nine regions used to investigate the variation of temperature and absorbing column within the diffuse emission. The regions are identified by the overlaid numbers with region 1 in the SW corner and region 9 in the NE corner.

expected from standard superbubble models (Weaver et al. 1977). The higher column densities seen in Table 6 and Fig. 9 for the regions to the SE, SW and W of the galaxy would suggest that these areas lie behind more absorbing material present in the disc of the galaxy and that the eastern and northern edges of the galaxy are tilted towards us as shown in the cartoon representation of the morphology of the galaxy in Fig. 13. Allowing for the position angle of NGC 4449, this would mean that the minor axis lies inclined to our line of sight (tilted both to the north and west) consistent with NGC 4449 being a Magellanic irregular that is inclined at 56.2° to our line of sight. The lower column density of region 3, in particular, would suggest that the X-ray emission in that region comes from material lying above the galactic disc.

5.1 Comparison with observations at other wavelengths

5.1.1 Star clusters

The galaxy contains many star clusters spread throughout the D_{25} ellipse and so star formation is not confined to a single well-defined region within the galaxy. The highest density of star clusters identified by Gelatt et al. (2001) is coincident with the peak seen in the diffuse X-ray emission at $\alpha = 12^{\rm h}28^{\rm m}11^{\rm s}.75$ and $\delta = +44°05'36''.1$. (The largest of the contours, labelled 3, in the lower panel of Fig. 14.) The peak in the diffuse emission to the SW of this at $\alpha = 12^{\rm h}28^{\rm m}09^{\rm s}.65$ and $\delta = +44°05'11''.5$ also has a large number of star clusters associated with it. It is likely that multiple superbubbles are being blown by the combined action of stellar winds and SN explosions from the

individual stars within these star clusters, leading to the increased diffuse X-ray emission from hot, shock-heated gas in these regions. This is supported by the complex morphology seen in the patterns of peaks in the X-ray emission shown in Fig. 12.

5.1.2 Comparison with Hα emission

Fig. 14 shows X-ray contours overlaid on an Hα map of NGC 4449 as well as the two separate images. This shows that the X-ray and Hα morphologies in the main body of the galaxy follow each other closely. The X-ray emission is also seen to extend out to the NW into what appears to be a hole in the Hα emission, bounded by filaments, labelled F in the lower panel. This could be a wind-blown superbubble or the escape of hot gas from a ruptured bubble in the form of a super-wind, labelled SB/SW. Ultraviolet observations (Hill et al. 1998) have identified regions along the northeastern edge of this hole, which show sequential star formation and this activity may be linked to the expansion of a super-bubble. As the bubble expands, it sweeps up and shock heats the ISM, leading to the formation of areas of increased density that can trigger star formation. In addition, the observed filamentary structure seen in Hα could be material from a ruptured bubble or entrained ISM material caught up in an outflow. A similar, if less pronounced effect also seems to be occurring to the SE, labelled SB. The extent of both emissions matches well, as can be seen by comparing the X-ray and Hα surface brightness slices shown for the same regions in Fig. 12. The only exception seems to occur to the west of the galaxy where the diffuse X-ray emission appears to extend beyond the region of high Hα intensity.

Table 6. Single or two-temperature fits for the nine regions of the diffuse emission (see the text for further details). Columns 1 and 2 contain the region numbers and counts for each region, respectively. Column 3 lists the column density for the absorbing gas within NGC 4449, column 4 the temperature(s) and column 5 the statistic for the fit for each region. Column 6 has the calculated absorption-corrected luminosities for each of the regions, the errors shown are from the 90 per cent confidence ranges (1.64σ) of the normalizations of the fits or are upper limits determined from these values where only one value is given. In all cases, the Galactic absorption column density was fixed at $N_H = 1.4 \times 10^{20}$ cm^{-3}.

Region	Counts	N_H (cm^{-2})	kT (keV)	χ^2/d.o.f.	L_X (erg s^{-1})
1	197 ± 21	2.87×10^{21}	0.19	17.9/14	$(2.29 \pm^{0.34}) \times 10^{38}$
2	246 ± 22	3.75×10^{21}	0.21	19.6/15	$(3.29 \pm^{0.45}) \times 10^{38}$
3	198 ± 21	4.38×10^{20}	0.45	22.7/14	$(3.52 \pm^{0.70}) \times 10^{37}$
4	440 ± 26	8.34×10^{20}	0.33, 1.03	36.3/20	$(1.09 \pm^{0.27}_{0.29}) \times 10^{38}$
5	1268 ± 39	1.28×10^{21}	0.27, 0.67	55.6/45	$(2.98 \pm^{0.79}_{0.71}) \times 10^{38}$
6	668 ± 30	1.08×10^{21}	0.39, 1.13	34.8/29	$(1.40 \pm^{0.27}_{0.38}) \times 10^{38}$
7	45 ± 17	4.69×10^{21}	0.27	4.20/7	$(5.44 \pm^{47.29}) \times 10^{37}$
8	442 ± 25	1.50×10^{21}	0.23, 0.58	19.5/20	$(1.33 \pm^{0.40}_{0.45}) \times 10^{38}$
9	294 ± 23	1.42×10^{21}	0.29, 1.93	11.96/17	$(8.94 \pm^{2.68}_{2.62}) \times 10^{37}$

Table 7. The $(m-s)/(m+s)$ hardness ratio for each of the nine regions. Column 1 lists the region numbers as shown in Fig. 8, columns 2 and 3 contain the count rates in the soft and medium bands, respectively, and column 4 gives the calculated hardness ratios. The softer emission is shown by the regions with more negative values.

Region	Count rate in soft band (count s^{-1})	Count rate in medium band (count s^{-1})	$\dfrac{(m-s)}{(m+s)}$
1	$(5.33 \pm 0.57) \times 10^{-3}$	$(8.81 \pm 0.77) \times 10^{-3}$	0.246 ± 0.070
2	$(7.21 \pm 0.67) \times 10^{-3}$	$(2.78 \pm 0.49) \times 10^{-3}$	-0.443 ± 0.091
3	$(5.39 \pm 0.59) \times 10^{-3}$	$(3.26 \pm 0.51) \times 10^{-3}$	-0.246 ± 0.093
4	$(11.0 \pm 0.80) \times 10^{-3}$	$(7.81 \pm 0.70) \times 10^{-3}$	-0.170 ± 0.057
5	$(31.5 \pm 1.20) \times 10^{-3}$	$(22.4 \pm 1.10) \times 10^{-3}$	-0.169 ± 0.031
6	$(14.4 \pm 0.90) \times 10^{-3}$	$(13.9 \pm 0.90) \times 10^{-3}$	-0.018 ± 0.046
7	$(1.29 \pm 0.37) \times 10^{-3}$	$(0.01 \pm 0.38) \times 10^{-3}$	-0.985 ± 0.570
8	$(10.7 \pm 0.80) \times 10^{-3}$	$(7.23 \pm 0.67) \times 10^{-3}$	-0.194 ± 0.059
9	$(5.33 \pm 0.58) \times 10^{-3}$	$(6.43 \pm 0.64) \times 10^{-3}$	0.094 ± 0.074

For the N to S and SW to NE slices, the overall profiles of the peaks are similar and they occupy a similar extent. The peaks of X-ray emission, in the northern half of these slices, tend to fall inside the peaks of Hα emission (i.e. they are slightly closer to the centre of the galaxy), with the intensity of the X-ray emission, in the north, being greatest close to the Hα peaks. This is the type of behaviour discussed by Strickland et al. (2002) in model 5 of the connection between X-ray and Hα emission, where the Hα emission is attributed to a swept-up shell that has cooled and surrounds a hot bubble of SN ejecta. These potential bubbles in the north of the galaxy, labelled B in the lower panel of Fig. 14, have diameters $\leqslant 1$ kpc and the most northern of the two does appear to be surrounded by an arc of increased intensity in the Hα emission, most clearly visible in the upper left-hand panel of Fig. 14. The increased intensity of the X-ray emission behind the Hα peaks would be due to conductive evaporation of the swept-up material, which increases the density and X-ray emissivity of the region where the hot gas and evaporated material mixes (Weaver et al. 1977). These two slices lie closest to the major axis of the galaxy and cut across the regions containing the highest densities of star clusters in the southern half of the galaxy. The association of the peaks is less clear on the southern side of both of these slices and this may well be a result of the overlapping and merging of many wind-blown bubbles from the large number of star clusters found there.

The slices running from NW to SE and W to E lie closest to the minor axis of the galaxy and cut across the bulging of the diffuse X-ray emission. The slices show what appear to be cavities in the Hα emission to both the NW and the E which are filled with X-ray emission, again suggesting the presence of wind-blown super-bubbles, while to the SE and W, the X-ray emission seems to lie outside the Hα emission, more suggestive of ruptured super-bubbles, particularly to the west as seen by the distribution of X-ray contours, labelled 1, in the lower panel of Fig. 14.

5.1.3 The large H I halo and H I clouds

The H I halo of NGC 4449 extends out to a radius of ~40 kpc (Bajaja et al. 1994) and its outer structure takes the form of enormous filaments and clouds (Hunter et al. 1998). The VLA observations of Hunter et al. (1998) and Hunter, van Woerden & Gallagher (1999), show that the inner regions consist of a concentration of gas centred on the optical galaxy that takes the form of seven large H I complexes embedded in a lower-density background, with the overall outline of the morphology bulging to the ESE and WNW as seen in the diffuse X-ray emission. Fig. 12 of Hunter et al. (1999), shows that the H I in the inner regions extends beyond the Hα filament seen to the WNW in Fig. 14 and beyond the bulge in the diffuse X-ray emission to the ESE. This could be indicative of the
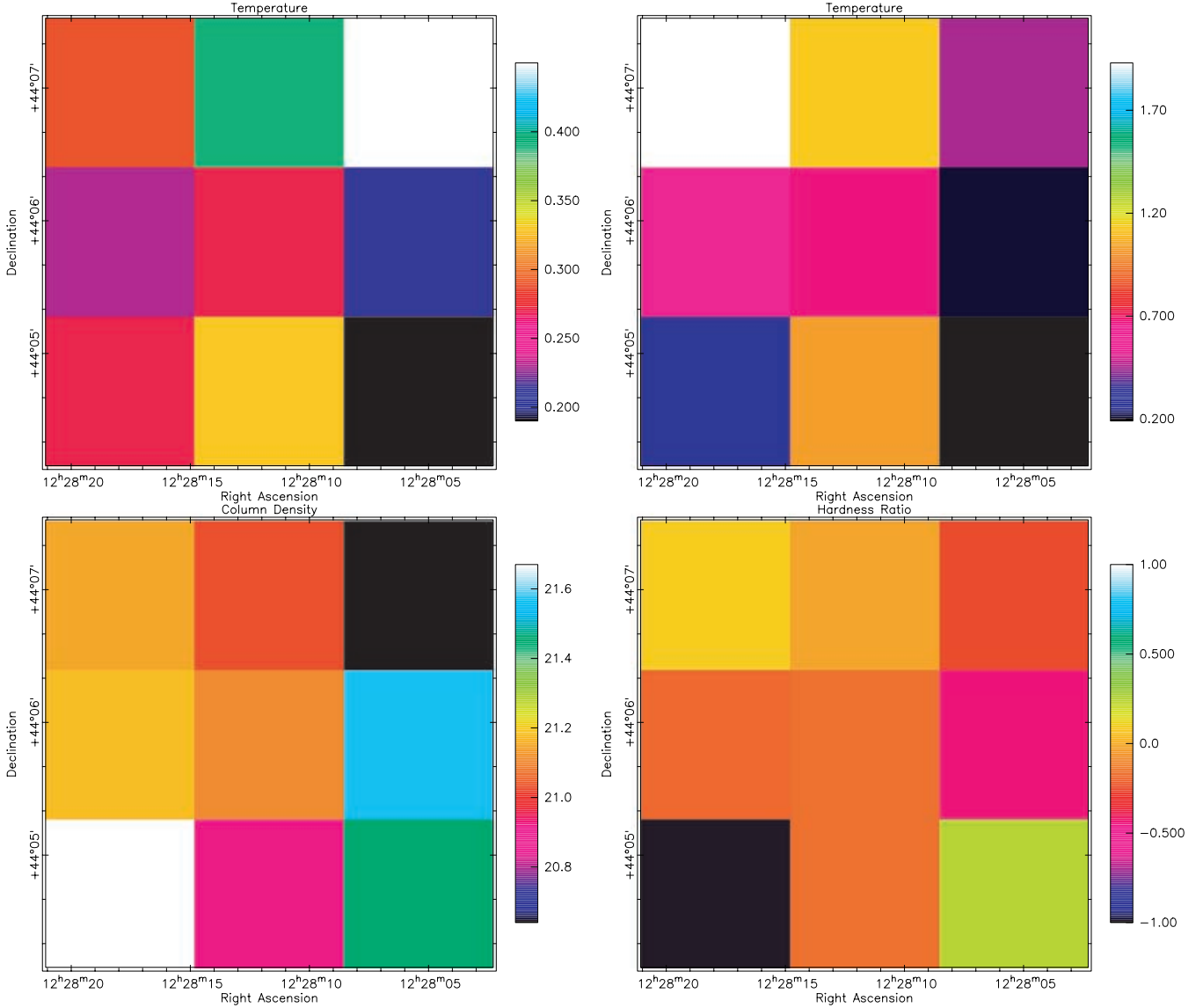
Figure 9. Colour-coded maps of the parameters investigated for variation within the diffuse emission. Top left: the temperature, in keV, of the softer thermal component within the nine regions. Top right: the temperature, in keV, of the hotter thermal component, where two were fitted. For the four regions with one temperature fits (regions 1, 2, 3 and 7), the soft thermal component temperature is shown. Bottom left: the logged value of the fitted column densities [log (N_H)], in cm^{-2}, for the nine regions. Bottom right: the calculated $(m - s)/(m + s)$ hardness ratio for the nine regions.

swept-up, compressed ambient interstellar medium lying outside the shells of two expanding super-bubbles. The regions of increased X-ray emission seen in the main body of the galaxy as well as lying close to regions of increased Hα emission also occupy areas where three of the H I clouds lie. This is suggestive of the increased H I density in these regions being caused by outflows from star clusters sweeping-up and compressing the ISM. The overall extent of the inner H I concentration is ∼9 kpc and it is embedded in an elliptical region of lower concentration with a major axis of ∼40 kpc from which streamers extend. By comparison, the extent of the diffuse X-ray-emitting region is ∼2.4 kpc along the major axis of the optical galaxy and ∼1.6 kpc in an approximate ESE–WNW direction. The optical extent of the galaxy as measured by the D_{25} ellipse is ∼4.35 × 3.35 kpc^2. Counter rotation is observed between the H I gas within the central region and that outside with the rotation velocity of the

inner gas being ∼18 km s^{-1} and that of the streamers seen in the halo ∼110 km s^{-1}. These two velocities and the distribution of the H I gas have implications for the potential of the hot gas, contained within any super-bubbles to escape. Modelling the potential of the galaxy as a simple spherically symmetric, truncated, isothermal potential (Binney & Tremaine 1987) then the escape velocity at a distance r from the centre of the galaxy is given by

$$v_{esc}(r) = 2^{1/2} v_{rot}[1 + \ln(r_t/r)]^{1/2} \text{ km s}^{-1}, \tag{1}$$

where v_{rot} is the maximum rotation velocity of the galaxy in km s^{-1} and r_t is the radius at which the potential is truncated. If the potential is truncated at the edge of the inner H I concentration at r_t ∼ 4.5 kpc then the escape velocity for the hot X-ray-emitting gas at 1.6 kpc from the centre, assuming v_{rot} ∼ 18 km s^{-1} would be ∼36 km s^{-1}. This is an upper limit as the value will decrease when
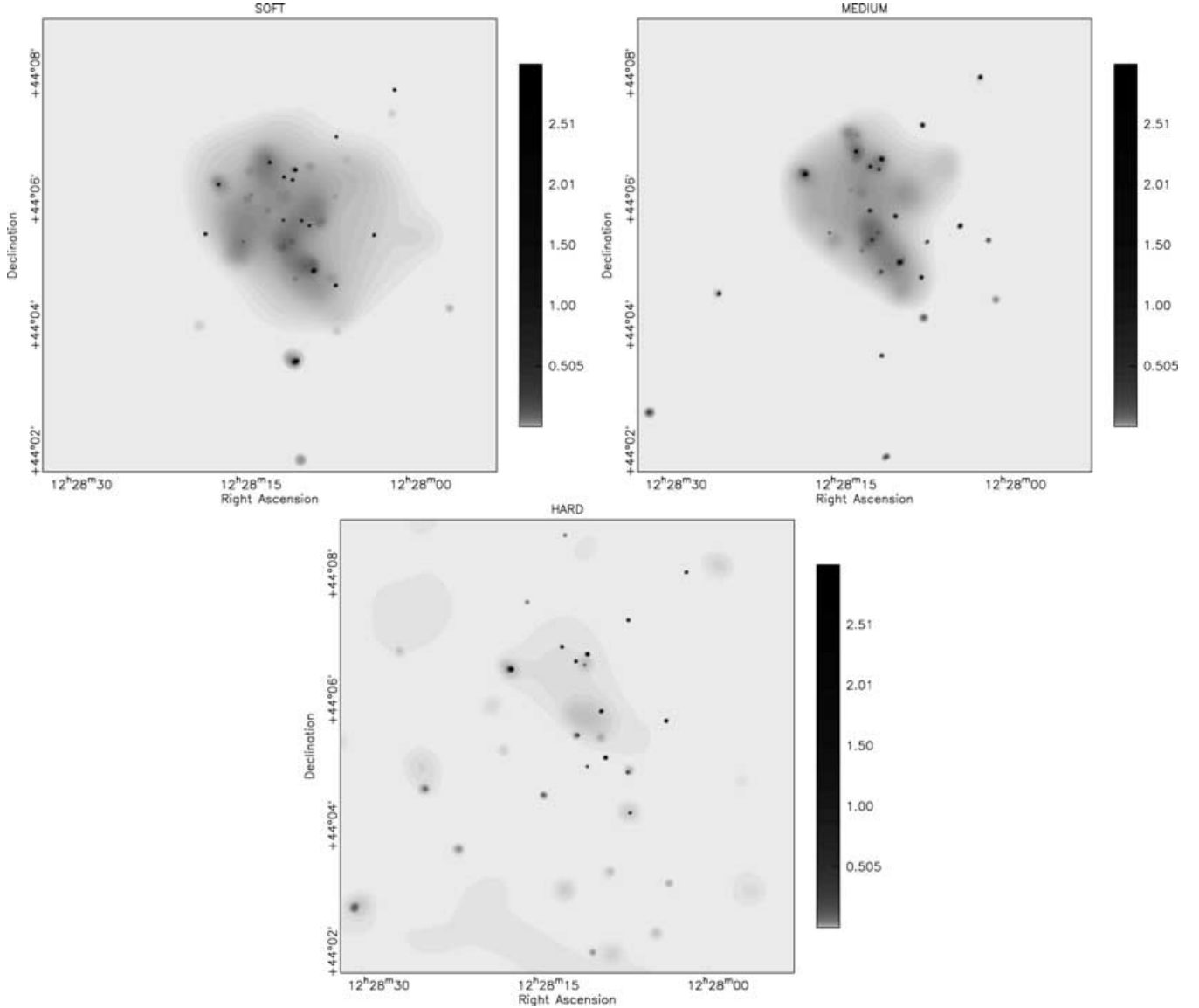
Figure 10. The three panels show smoothed images of the soft (0.3–0.8 keV), medium (0.8–2.0 keV) and hard (2.0–8.0 keV) energy bands, with the same grey-scale scaling, highlighting the differences in spatial distribution between the bands for the diffuse emission and the different spectral characteristics of the point sources.

the extent of the hot gas is deprojected. A similar calculation for the potential truncated at the edge of the H I halo at ∼40 kpc, with v_{rot} ∼ 110 km s^{-1} gives an upper value for v_{esc} ∼ 320 km s^{-1}. In the absence of radiative cooling, hot gas can escape the potential of the galaxy if its temperature is greater than

$$T_{esc} = 1.5 \times 10^5 (v_{100})^2 \text{ K,} \qquad (2)$$

where T_{esc} is the temperature required for the gas to exceed the escape velocity of the galaxy and v_{100} is the escape velocity in units of 100 km s^{-1} (Martin 1999). The two escape velocities determined above have corresponding escape temperatures of 1.94×10^4 and 1.54×10^6 K, respectively. From the gas parameters given in Table 5 both the soft and medium components of the hot gas have temperatures in excess of these values. Eventual escape of the metal-enriched SN ejecta contained within the super-bubbles seems possible for NGC 4449 but the distribution of the gas in the extended halo of the galaxy could be as important as gravity

in controlling whether the hot gas escapes or not. The presence of streamers of H I rather than a homogeneous distribution of material can facilitate the escape of hot gas through the gaps between the streamers.

5.1.4 Radio–X-ray agreement

The 5-GHz VLA observation (Bignell & Seaquist 1983) identifies the known SNR (source 15) in NGC 4449 with the most intense peak of the radio emission. The next three most intense peaks on this radio observation also lie close to sources in our data (sources 10, 18 and 23) that have all been flagged as possible SNRs, although none convincingly. In addition, these radio peaks are coincident with the three brightest peaks of emission on the Hα map, where intense star formation is occurring and where the presence of SNRs in star clusters is to be expected.
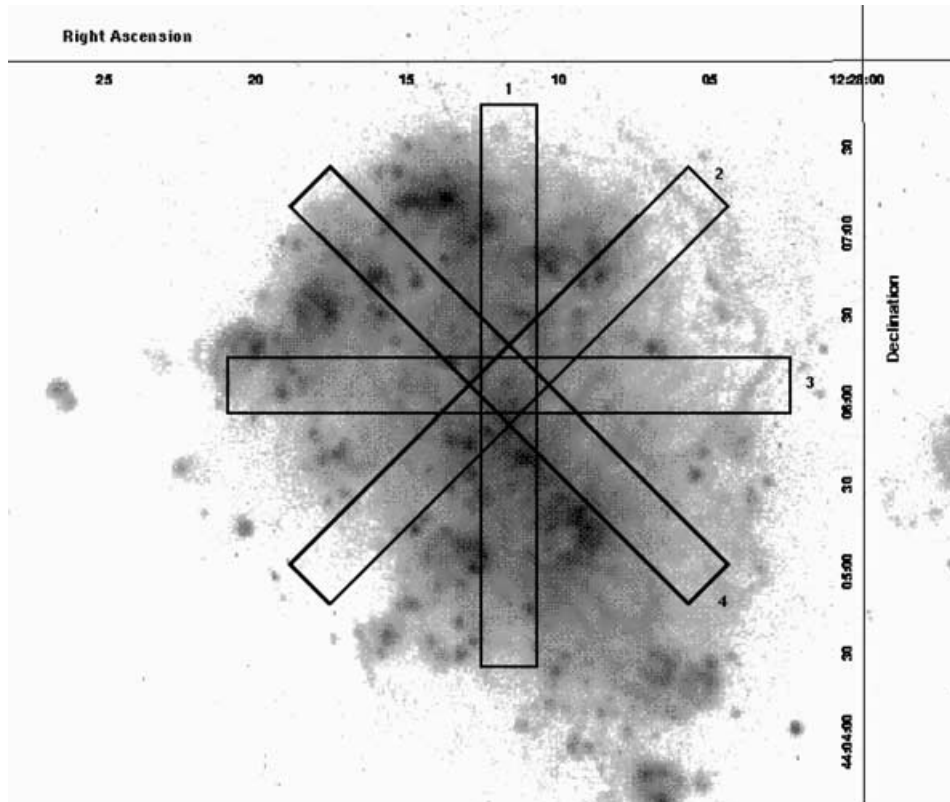
Figure 11. Hα image of NGC 4449 with the positions of the four slices overlaid. Each slice is centred on $\alpha = 12^h28^m11^s.7$ and $\delta = +44°06'04''.7$, has a length of 200 arcsec and a width of 20 arcsec. Slice 1 runs from north to south, slice 2 from northwest to southeast, slice 3 from west to east and slice 4 from southwest to northeast. The resulting X-ray and Hα profiles from these four slices are shown in Fig. 12.

5.2 Implications of the calculated gas parameters on the fate of NGC 4449

The presence of what appears to be a developing super-wind in this dwarf galaxy can have dramatic effects on its evolution. The lower gravitational potential of dwarfs makes the possibility of losing newly synthesized metals and swept-up ISM material more likely. As such it is worth considering the impact that the western super-bubble/super-wind might have on NGC 4449. The position of the super-bubble suggests that its origins may lie in three OB associations identified by Hill et al. (1994), that lie in the SW region of the main body of the galaxy where the highest density of star clusters is seen. The ages of these three OB associations were found to be 5.9, 6.2 and 6.7 Myr, while their corresponding masses were 1.6 $\times 10^5$, 6.3 $\times 10^5$ and 2.5 $\times 10^6$ M$_\odot$. The extent that the diffuse emission extends from the position of these OB associations is ∼1.7 arcmin or 1.4 kpc for our assumed distance down to a flux density level of 0.65×10^{-13} erg s^{-1} cm^{-2} arcmin^{-2}. Assuming an average age for the OB associations of 6.3 Myr then to have travelled this distance the expansion velocity of the bubble has to be ∼220 km s^{-1}. This will be an underestimate since the deprojected distance will be greater than that assumed and also the presence of a density gradient in the halo above the disc of the galaxy will lead to acceleration of the super-wind. Furthermore, from the calculated gas temperature of the soft component of the emission given in Table 5, a simple energy conservation analysis would give the average speed of a particle to be ∼280 km s^{-1}, which is in good agreement. At these sorts of velocities, it would take ∼200 Myr for the super-wind to reach a distance of 40 kpc and thus escape the H I halo. This is of

the same order as the radiative cooling time for the soft component of the diffuse emission and again suggests that the huge H I halo of NGC 4449 may allow it to retain its newly synthesized metals and ISM. The likelihood that the H I halo will prevent blowout is also found when the criterion for blow-out defined by Mac Low & McCray (1988) is applied to NGC 4449. This is based on the parameter Λ, defined as the dimensionless rate of kinetic energy injection, given by

$$\Lambda = 10^4 L_{\mathrm{mech},41} H_{\mathrm{kpc}}^{-2} P_4^{-3/2} n_0^{1/2}, \tag{3}$$

where $L_{\mathrm{mech},41}$ is the mechanical energy luminosity in units of 10^{41} erg s^{-1}, H_{kpc} is the galaxy scaleheight in kpc, P_4 is the initial pressure of the ISM in units of $P/k = 10^4$ K cm^{-3} and n_0 is its initial density. For blow-out to occur, the condition $\Lambda > 100$ has to be satisfied. For the whole of the X-ray-emitting gas, the thermal energy content given in Table 5 is 2.46×10^{55} erg. Assuming that this is the result of complete thermalization of the kinetic energy of the stellar winds and SN ejecta, occurring over the lifetime of the OB associations, then L_{mech} for the whole galaxy is ∼1.2×10^{41} erg s^{-1} (a similar estimate to that of 3×10^{41} erg s^{-1} obtained by Della Ceca et al. 1997, from the Leitherer & Heckman 1995, starburst models). The actual thermalization will be less than complete, but as argued by Strickland & Stevens (2000), will most likely be between 10 and 100 per cent, meaning that the L_{mech} value above could be greater by up to an order of magnitude. Assuming the initial ISM pressure was similar to that of our Galaxy then $P_4 \sim 1$ and a comparison with the gas pressures for the hot gas given in Table 5 shows that they are an order of magnitude higher, which is to be expected for an adiabatically expanding overpressured bubble. As a further assumption, the
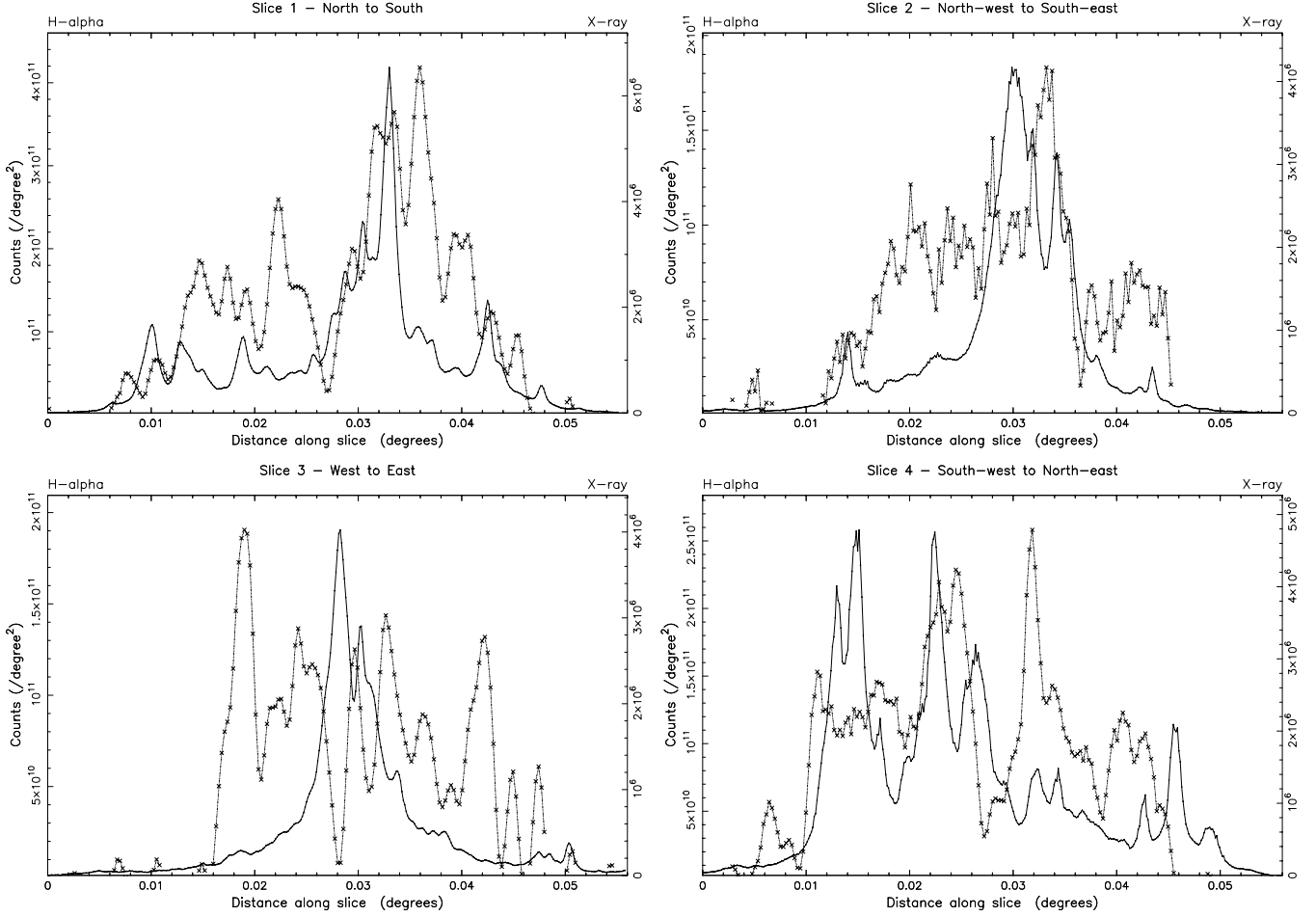
Figure 12. X-ray surface brightness slices (crosses and dashed curves) overlaid on the Hα surface brightness slices (solid curves). The *y*-axes on the left of each panel gives the counts deg^{-2} for the Hα slices while those to the right are the values for the X-ray slices. Although these axes are on very different scales they do allow a comparison to be made of the spatial distribution of X-ray and Hα peaks along each of the slices. All the slices are centred on $\alpha = 12^h28^m11^s7$ and $\delta = +44°06'04''.7$, located 0.028° along the slice, have a length of 200 arcsec and a width of 20 arcsec. This position coincides with the central trough in the diffuse X-ray emission indicated by the small central contour labelled 2 at that position in Fig. 14.

hot gas will be at a lower density than the initial ambient density of the ISM and an order of magnitude change will be assumed from the average value in Table 5. The result of using these figures in the above equation with $\Lambda = 100$ means that the scaleheight for NGC 4449 has to be $\leqslant$9.5 kpc, which is somewhat less than the size of the H I halo. In addition this figure will be an overestimate since $L_{\rm mech}$ was estimated from the energy content of the whole volume assumed to be occupied by the diffuse emission. The volume of the western superbubble is only ~10 per cent of the total volume and if the ambient ISM density is assumed to be closer to that of the hot gas then again the scaleheight will decrease. If the halo has holes in it, as suggested by the presence of streamers rather than a homogeneous distribution, then escape is more likely.

If escape occurs then the amount of mass lost may affect the ability of NGC 4449 to continue star formation. Assuming the super-bubble has around a tenth of the volume of the diffuse emission and as such around a tenth of the mass given in Table 5 then over 6.3 Myr, the average mass injection rate will have been 0.14 M$_\odot$ yr^{-1}, a figure which is similar to that predicted for Mrk 33 (Summers, Stevens & Strickland 2001), another dwarf galaxy that may be developing a super-wind. If this rate of mass injection was maintained while the super-bubble/super-wind expanded to the edge of the H I halo over

a time-span of ~200 Myr then the total amount of mass it would contain would be ~2.5 × 10^7 M$_\odot$. This value is greater than the mass contained within the three OB associations (~3.3 × 10^6 M$_\odot$) and the time-scale is also in excess of the lifetimes of the massive stars found there, so unless a large amount of mass-loading from ISM material is to occur this would be an overestimate of the mass that the super-bubble/super-wind would contain on escape. Compared with the total mass of NGC 4449 of ~4 × 10^{10} M$_\odot$ this is only about 0.1 per cent of the total mass of the galaxy. As the time-scale required is in excess of the lifetimes of the massive stars then the energy-injection rate would also decrease before escape was attained, suggesting that the bubble expansion is likely to stall. Hence it seems unlikely that the development of this super-bubble/super-wind in NGC 4449 will have a great deal of effect on the ability of the galaxy to both retain its products of star formation and continue star formation in the future.

5.3 Morphology of NGC 4449

Fig. 13 shows a cartoon of the possible morphology of NGC 4449 and, in particular, shows how the diffuse X-ray, Hα and H I emissions may be associated with each other, at the maximum extent of the
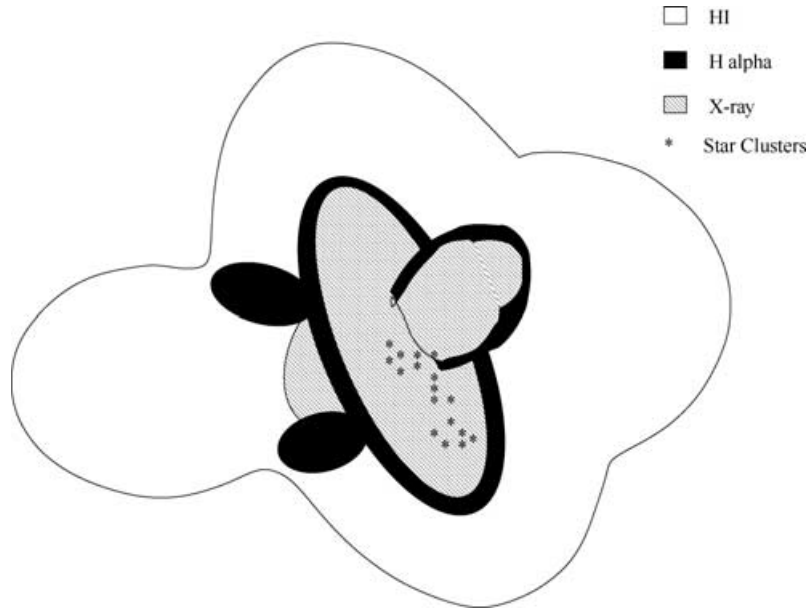
Figure 13. Cartoon representation of the relationship between the X-ray, Hα and H I morphologies of NGC 4449 and the approximate positions of the starclusters in the densest groups (from Gelatt et al. 2001). The extent of the X-ray and Hα emissions were determined from a comparison of matched images of the X-ray data and the Hα image. The extent of the H I shown is estimated from fig. 12 of Hunter et al. (1998) which shows H I contours overlaid on an image of the same Hα data. The structure shown in the X-ray bubble to the NW represents the extension of the X-ray emission seen in this direction in Fig. 14 that may actually extend beyond the Hα filament seen there and as such may be indicative of the escape of hot gas from a ruptured super-bubble in the form of a super-wind.

X-ray and Hα emission, if the galaxy is assumed to have a bi-polar outflow in the form of two wind-blown super-bubbles along its minor axis. The stars represent the approximate positions of the starclusters in the two densest populated regions, as identified by Gelatt et al. (2001). The structure shown in the X-ray emission in the NW super-bubble may be indicative of the bubble rupturing and X-ray emission beginning to extend beyond the Hα emission as is suggested in the X-ray and Hα slices of Fig. 12. A comparison of the NW–SE and W–E slices that run along the northern and southern edges of the bubble, respectively, suggest that the X-ray emission is bounded by the Hα emission to the north but not to the south. A similar picture is seen to the east of the galaxy where the emission to the east seems to be bounded, whilst that to the SE is unbounded. In the regions of intense star formation to the south, there are several peaks of emission in both the X-ray and Hα bands, indicative of a confused morphology where the presence of several wind-blown bubbles is to be expected and their overlapping both physically and in projection will make individual bubbles impossible to identify. To the north, the presence of two bubbles with diameters $\leqslant 1$ kpc seems to be indicated in the surface brightness slices of Fig. 12. The H I outline in Fig. 13 represents the extent of the inner H I cloud complexes and H I ISM down to a column density of 15×10^{20} cm^{-2} as shown in figs 10 and 12 of Hunter et al. (1999). Comparing these two figures with Fig. 14 above, although obviously different in size, all three types of emission do appear to have a similar outline to their morphologies.

6 SUMMARY AND CONCLUSIONS

In summary, we have presented an analysis of the X-ray data obtained from a 30-ks observation, of the Magellanic irregular, star-burst galaxy NGC 4449 using the *Chandra* satellite. We find X-ray emission from 32 discrete point sources in the S3 chip data with 24

of them lying within the optical extent of the galaxy, as measured by the extent of the D_{25} ellipse. Some of these can be clearly identified as SNRs, others as XRBs and there are also several SSS. We calculate an age for the previously identified SNR (source 15) of 270 yr and a density for the medium into which it has exploded of being $\leqslant 200$ cm^{-3}. The bright SSS (source 14) is a candidate for being a white dwarf binary system, while the source exhibiting the highest count rate during the observation (source 27) shows long-term variability and is most likely an HMXB.

The galaxy has a very extended distribution of H I, but the inner concentration of H I has an overall general morphology which also follows that of the X-ray emission but on a larger scale. The H I complexes within the inner region could be the result of outflows from the multiple star clusters in the starburst of NGC 4449 compressing and driving the ambient ISM of the galaxy away from the centre, both along the minor axis of the galaxy and above regions of increased star formation within the disc. The overall extent of the inner H I concentration is ∼9 kpc, that of Hα is ∼4.35 × 3.35 kpc^2 and that of the X-ray emission is ∼2.5 × 1.6 kpc^2, with this central region being embedded within a huge H I halo extending out to ∼40 kpc.

The total X-ray luminosity of NGC 4449 in the 0.3–8.0 keV energy band is $(2.46 \pm^{0.19}_{0.20}) \times 10^{39}$ erg s^{-1} cm^{-2}. Of this, ∼60 per cent is due to resolved point sources and the rest is due to diffuse X-ray emission. As suggested by this analysis and those of other starburst galaxies (e.g. NGC 253, Strickland et al. 2002; NGC 1569, Martin et al. 2002, Della Ceca et al. 1996; NGC 4449, Della Ceca et al. 1997), the diffuse X-ray emission is emerging as a multiphase environment requiring complex spectral models, which the spectral resolution of even current X-ray telescopes cannot meaningfully constrain. We thus conclude that the diffuse X-ray emission contains gas at, at least two different temperatures and evidence for unresolved point sources. The fitted gas temperatures are 0.28 ± 0.01
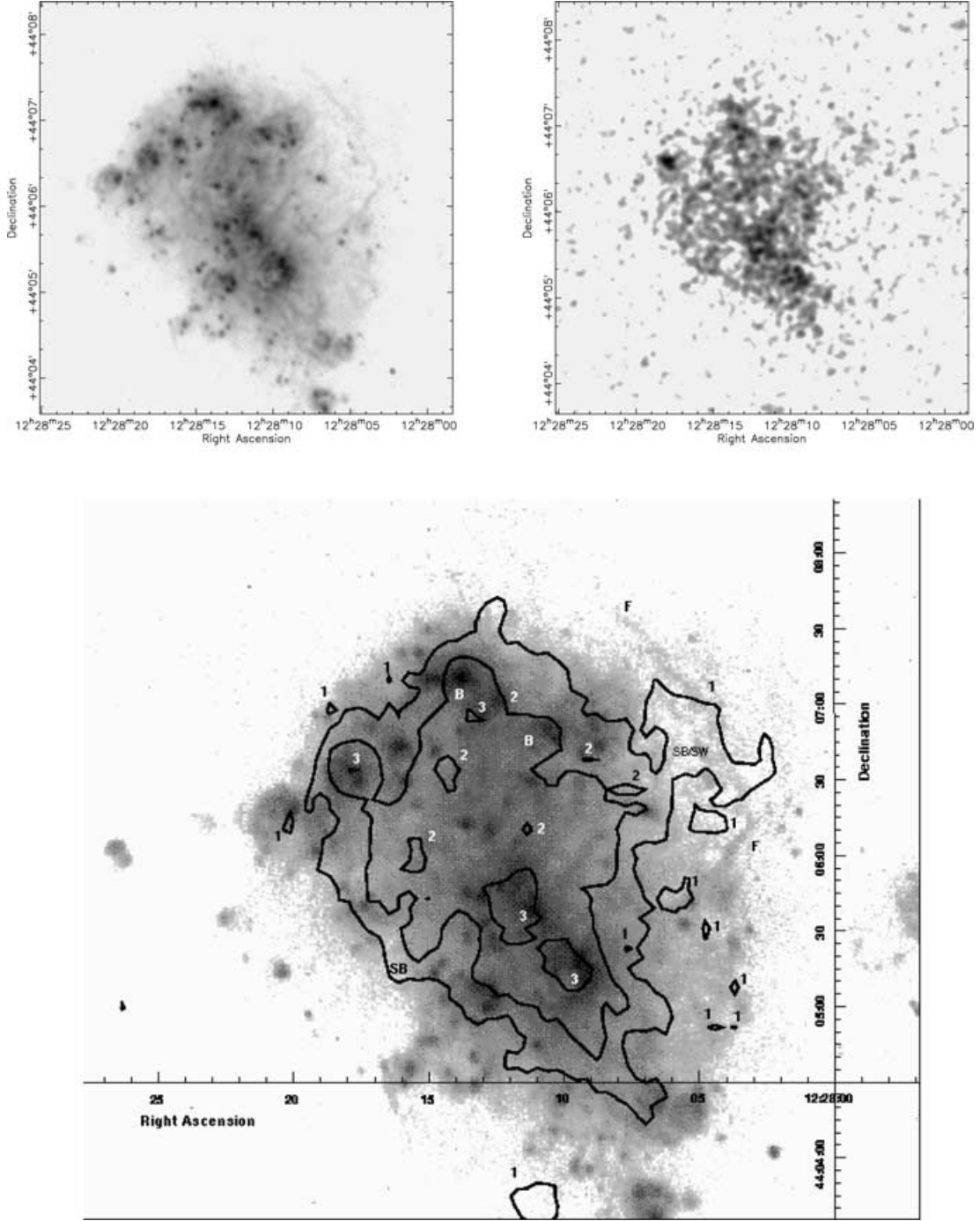
Figure 14. Top left: Hα grey-scale image of NGC 4449. Top right: point source and background-subtracted diffuse X-ray grey-scale image of NGC 4449 on the same spatial scale as the Hα image and with the same smoothing as in Fig. 8. Bottom: X-ray contours from the image shown top right overlaid on the Hα image of NGC 4449. The X-ray contours labelled 1 are at a flux density of 0.65×10^{-13} erg s^{-1} cm^{-2} arcmin^{-2}. Those labelled 2 are at a flux density of 1.3×10^{-13} erg s^{-1} cm^{-2} arcmin^{-2} and those labelled 3 are at 2.6×10^{-13} erg s^{-1} cm^{-2} arcmin^{-2}. The background flux density level is $\sim 0.25 \times 10^{-13}$ erg s^{-1} cm^{-2} arcmin^{-2}. Also labelled are the filaments (F), bubbles (B), super-bubbles (SB) and super-wind (SW) discussed in the text.

and 0.86 ± 0.04 keV for the soft and medium components, respectively, and their respective absorption-corrected fluxes in the 0.3–8.0 keV band are $(6.66^{+0.34}_{0.35}) \times 10^{-13}$ erg s^{-1} cm^{-2} and $(2.20^{+0.26}_{0.25}) \times 10^{-13}$ erg s^{-1} cm^{-2}, corresponding to luminosities of $(6.83^{+0.35}_{0.36}) \times 10^{38}$ erg s^{-1} and $(2.26^{+0.27}_{0.26}) \times 10^{38}$ erg s^{-1}. This diffuse emission seems to be more heavily absorbed in the SW of the galaxy and shows a higher temperature in the central and eastern regions

consistent with NGC 4449 being an inclined Magellanic irregular galaxy, with its minor axis inclined to the north and west of our line of sight. The morphologies of the X-ray and Hα emissions from the galaxy follow each other closely and the X-ray emission appears to fill cavities in the Hα emission to the NW and E – highly suggestive of wind-blown super-bubbles extending along the minor axis of the galaxy. To the SE and W, the X-ray emission seems to lie outside the

Hα emission and this may indicate the developing of a super-wind from the rupture of the super-bubbles. The large number of peaks in emission seen in both the Hα and diffuse X-ray data indicates a complex morphology within the main body of the galaxy. Regions containing small ($\leqslant 1$ kpc) bubbles of X-ray emission surrounded by shells of Hα emission are seen, that are produced by the combined action of stellar winds and SN explosions from massive stars, shock-heating both the stellar ejecta and ISM and sweeping it into shells as the ejecta drives its way out of star clusters.

The hot X-ray-emitting gas has a total thermal energy content of $\sim 2.5 \times 10^{55}$ erg and a total mass of $\sim 9.0 \times 10^6$ M$_\odot$. The super-bubble/super-wind extending to the WNW of the galaxy occupies around 10 per cent of the total volume occupied by the hot gas (assuming a filling factor of 1). The origin of this outflow appears to be the concentration of star clusters observed in the SW region of the galaxy disc (Hill et al. 1994). At present, the average energy injection rate for the whole galaxy is $\sim 1.2 \times 10^{41}$ erg s^{-1} and the mass injection rate into the super-bubble is ~ 0.14 M$_\odot$ yr^{-1}. It seems unlikely that this bubble can escape from the huge H$\,$I halo at its current estimated expansion speed of ~ 220 km s^{-1}, as the time required is in excess of the lifetimes of the massive stars of the star clusters and comparable to the radiative cooling time of the soft component of the diffuse emission, whilst the expansion velocity is less than the estimated escape velocity from the H$\,$I halo. However, the current temperatures of both gas components imply that they are capable of escaping the gravitational potential of the galaxy and so venting metal-enriched, hot gas into the IGM. The crucial factors are the time for which energy injection can be maintained and the actual distribution of H$\,$I in the halo of NGC 4449. The less homogeneous the distribution, the more likely the possibility that some of the hot gas can escape. At current mass injection rates, the total mass loss would be <1 per cent of the mass of the galaxy and as such would not have a catastrophic effect on NGC 4449.

REFERENCES

Aaronson M., Mould J., 1983, ApJ, 265, 1
Bajaja E., Huchtmeier W.K., Klein U., 1994, A&A, 285, 385
Balick B., Heckman T., 1978, ApJ, 226, L7
Bignell R.C., Seaquist E.R., 1983, ApJ, 270, 140
Binney J., Tremaine S., 1987, Galactic Dynamics. Princeton Univ. Press, Princeton
Blair W.P., Kirshner R.P. Winkler P.F., Jr, 1983, ApJ, 272, 84
Blair W.P., Raymond J.C., Fesen R.A., Gull T.R., 1984, ApJ, 279, 708
Böker T., van der Marel R.P., Mazzuca L., Rix H.-W., Rudnick G., Ho L.C., Shields J.C., 2001, AJ, 121, 1473
Bothun G.D., 1986, AJ, 91, 507
Brandt W.N. et al., 2001, AJ, 122, 2810
Della Ceca R., Griffiths R.E., Heckman T.E., MacKenty J.W., 1996, ApJ, 469, 662
Della Ceca R., Griffiths R.E., Heckman T.E., 1997, ApJ, 485, 581
de Vaucouleurs G., de Vaucouleurs A., Corwin J.R., Buta R.J., Paturel G., Fouque P., 1991, Third Reference Catalogue of Bright Galaxies, Version 3.9. Univ. Texas Press, Austin
Ebisawa K. et al., 2001, ApJ, 550, 1007
Gelatt A.E., Hunter D.A., Gallagher J.S., 2001, PASP, 113, 142
Hartmann L.W., Geller M.J., Huchra J.P., 1986, AJ, 92, 1278
Hill R.S., Home A.T., Smith A.M., Bruhweiler F.C., Cheng K.-P., Hintzen P.M.N., Oliversen R.J., 1994, ApJ, 430, 568
Hill R.S. et al., 1998, ApJ, 507, 179
Hunter D.A., Gallagher J.S., 1990, ApJ, 362, 480
Hunter D.A., Gallagher J.S., 1997, ApJ, 475, 65
Hunter D.A., Thronson H.A., Jr, 1996, ApJ, 461, 202
Hunter D.A., Wilcots E.M., van Woerden H., Gallagher J.S., Kohle S., 1998, ApJ, 495, L47
Hunter D.A., van Woerden H., Gallagher J.S., 1999, AJ, 118, 2184
Karachentsev I.D., Drozdovsky I.O., 1998, A&AS, 131, 1
Klein U., Hummel E., Bomans D.J., Hopp U., 1996, A&A, 313, 396
Leitherer C., Heckman T.M., 1995, ApJS, 96, 9
Mac Low M.-M., McCray R., 1988, ApJ, 324, 776
Martin C.L., 1997, ApJ, 491, 561
Martin C.L., 1999, ApJ, 513, 156
Martin C.L., Kobulnicky H.A., Heckman T.M., 2002, ApJ, 574, 663
Patnaude D.J., Fesen R.A., 2003, ApJ, 587, 221
Seaquist E.R., Bignell R.C., 1978, ApJ, 226, L5
Strickland D.K., Stevens I.R., 2000, MNRAS, 314, 511
Strickland D.K., Heckman T.M., Weaver K.A., Dahlem M., 2000, AJ, 120, 2965
Strickland D.K., Heckman T.M., Weaver K.A., Hoopes C.G., Dahlem M., 2002, ApJ, 568, 689
Summers L.K., Stevens I.R., Strickland D.K., 2001, MNRAS, 327, 385
Thronson H.A., Jr, Hunter D.A., Telesco C.M., Harper D.A., Decher R., 1987, ApJ, 317, 180
Vogler A., Pietsch W., 1997, A&A, 319, 459
Weaver K.A., 2001, in Knapen J.H., Beckman J.E., Sholsman I., Mahoney T.J., eds, ASP Conf. Proc. Vol. 249, The Central kpc of Starbursts and AGN, The La Palma Connection. Astron. Soc. Pac., San Francisco, p. 389
Weaver R., McCray R., Castor J., Shapiro P., Moore R., 1977, ApJ, 218, 377
Yokogawa J., Imanishi K., Koyama K., Nishiuchi M., Mizuno M., 2002, PASJ, 54, 53
Zezas A., Fabbiano G., Prestwich A., Ward M., Murray S., 2001, in Knapen J.H., Beckman J.E., Sholsman I., Mahoney T.J., eds, ASP Conf. Proc. Vol. 249, The Central kpc of Starbursts and AGN, The La Palma Connection. Astron. Soc. Pac., San Francisco, p. 425

This paper has been typeset from a T$_{\rm E}$X/L$^{\rm A}$T$_{\rm E}$X file prepared by the author.